Contributions to Mineralogy and Petrology (2025) 180:3
https://doi.org/10.1007/s00410-024-02195-0

ORIGINAL PAPER

Magmatic evolution and magma chamber conditions of the Alpehué tephra from Sollipulli Volcano, Andean Southern Volcanic Zone, Chile/Argentina

Armin Freundt[1] · **Karen Strehlow**[1,2] · **Steffen Kutterolf**[1] · **Julie Christin Schindlbeck-Belo**[1]

Received: 18 March 2024 / Accepted: 26 November 2024

Abstract

The trachydacitic Alpehué tephra from Sollipulli volcano (Andean Southern Volcanic Zone), consists of ignimbrite and fallout from a Plinian eruption about 3000 years ago. It is mainly composed of (1) crystal-rich pumice and ash but also contains (2) chilled knobbly basaltic lava clasts and (3) mostly highly inflated glomerocrystic fragments with high crystal-glass ratios interpreted to represent a crystal mush zoned from basaltic to dacitic bulk compositions. Knobbly lava clasts are of three types: (a) a very phenocryst-poor basalt, (b) a basalt with large, unzoned olivine and plagioclase phenocrysts and glomerocrysts, and (c) mixtures of microcrystalline basalt with various fragments, glomerocrysts and crystals derived from a crystal mush. Clast type (4) in the tephra is banded pumices in which the three magmatic components occur variably mingled. Thermobarometry and petrographic observations, particularly presence or absence of amphibole, constrain an upper-crustal succession of a lower basaltic reservoir, a zoned basaltic to dacitic crystal mush reservoir, and a separate trachydacite magma chamber on top. All Alpehué magmatic components form a coherent liquid line of descent which supports the interpretation that the crystal mush reservoir is a gradually solidifying magma chamber, not the result of large-scale crystal-liquid segregation. The trachydacite magma may originally have formed as melt escaping from the crystal-mush reservoir but subsequently underwent a long and complex evolution recorded in large strongly zoned plagioclase phenocrysts including resorption horizons. The ascending mafic magmas collected samples from the crystal mush body and intruded the trachydacite reservoir. The phenocryst-poor basalt (a) arrived first and entrained and partially resorbed plagioclase from the host magma. The phyric basalt (b) arrived later and did not resorb entrained plagioclase before eruption. Estimated cooling times, plagioclase resorption times and ascent rates avoiding amphibole breakdown limit the duration of these pre-eruptive processes to not more than a few days.

Keywords Phyric pumice · Crystal mush · Magma chamber evolution · Mafic replenishment · Thermobarometry

Introduction

Since magmatic differentiation by crystallization had been recognized about 100 years ago (e.g., Bowen 1928) and petrologic studies of layered intrusions provided evidence for crystal-melt segregation (e.g., Wager et al. 1960), the processes leading to such separation have been extensively discussed. In the last century, the focus was on melt-dominated magma chambers in which crystal-melt segregation was achieved by crystal settling or floating, by crystal-rich gravity currents, or by side-wall crystallization combined with compositional convection (e.g., McBirney and Noyes 1979; Huppert and Sparks 1984; Tait et al. 1984; Martin and Nokes 1988; Weinstein et al. 1988; Tait and Jaupart 1992). In these magma chamber models, crystal mushes played a role in marginal crystallization and accumulation zones but differentiated magmas mainly formed by convective processes within the (mostly open-system) magma chamber (Marsh 1989). More recent techniques of single-crystal radiometric

---

Communicated by Othmar Müntener.

✉ Armin Freundt
afreundt@geomar.de

[1] GEOMAR Helmholtz Centre for Ocean Research Kiel, 24148 Kiel, Germany

[2] Mitiga Solutions S.L, Barcelona 08039, Spain

and diffusion dating revealed both, phenocrysts recording chamber evolution within a short time span before eruption (~ 100 years; Costa et al. 2008; Druitt et al. 2012), and crystals which had resided in an active, hot magmatic region for up to a few 100 kyrs (Claiborne et al. 2010; Cisneros de Leon et al. 2021). These and other findings have led to a new concept of magmatic systems which are dominated by a vertically extensive body of crystal mush, possibly occupying the entire depth of the crust, from which interstitial melt escapes to form transient reservoirs of crystal-poor, evolved melt at their top which eventually erupt (see reviews by Cashman et al. 2017; Holness et al. 2019; Sparks et al. 2019).

Next to indirect geochemical and geophysical evidence for extensive mush zones, co-genetic less-evolved or mafic, variably crystal-rich enclaves and cumulate fragments in evolved volcanic deposits provide direct samples from regions of the magmatic system outside the erupted magma body. For example, Winslow et al. (2022) report cumulate and lava enclaves in Cordón Caulle rhyolite which have only basaltic compositions. They thus infer an entirely basaltic cumulate mush body invaded and penetrated by basaltic magma from depth, and capped by a layer of crystal-poor rhyolite representing escaped interstitial melt of the mush. On a two orders of magnitude larger volume scale, Rooyakkers et al. (2018) interpreted basaltic to dacitic enclaves in the rhyolitic Oruanui tephra to show that within ~ 10^5 years (Allan et al. 2017) the reservoir became zoned from basal rigid cumulate mush through a transition zone of lower strength and crystallinity to the fluid-dominated rhyolite that ultimately erupted. Intruding mafic magma diked through the rigid mush but disintegrated in, and mixed with the transition zone. Rather than forming distinct crystal-rich blocks, material from a crystal mush can also become well mixed into erupted magma to form a compositional subpopulation (and mostly cores) of the phenocrysts (Cooper and Wilson 2014). Plutonic fragments in andesites from the Lesser Antilles arc, ranging from basaltic to rhyolitic bulk-rock compositions and including glass-bearing incompletely solidified samples, have been interpreted to represent a heterogeneous mid-upper crustal crystal mush hosting a variety of melt compositions that blended to form compositionally less diverse erupted magmas (Cooper et al. 2019).

These examples show that size, structure and composition of crystal mushes can differ significantly between magmatic systems. The ~8 km^3 trachydacitic Alpehué tephra, which erupted ~ 3 kyrs ago from Sollipulli volcano at the Chile-Argentina border, contains both mafic enclaves and variably inflated glomerocrystic fragments, as well as mixtures thereof, which we here investigate in order to constrain the magmatic system that was associated with the main evolved magma reservoir. The crystal-rich nature of the Alpehué trachydacitic pumice contrasts with crystal-poor silicic melt thought to be extracted from a mush zone (Bachmann and Bergantz 2004, 2008). We use petrographic, geochemical and thermobarometric constraints to decipher the spatial and temporal interactions between the different components of this magmatic system.

Geological background

Sollipulli volcano is located in the Andean Southern Volcanic Zone (SVZ) at the border between Chile and Argentina (38.97° S and 71.52° W), approximately 25 km behind the volcanic front which is marked by the neighbouring volcanoes Villarrica and Llaima (Fig. 1a). The basement of Sollipulli consists of Jurassic sedimentary rocks and granitoids, Cretaceous to Miocene volcanic-sedimentary deposits including Miocene granitoids, and Quaternary volcanic rocks. Sollipulli volcano lies at the eastern end of the Pleistocene (< 1.8 Ma) Nevados del Sollipulli, an E-W extending field of glacially eroded lavas, domes and breccias (Naranjo et al. 1993). The volcanic edifice of Sollipulli comprises an older (< 0.5 Ma), intensely eroded caldera and a second, younger, ~4 km wide caldera, which is embedded in the northeastern rim of the older one (Naranjo et al. 1993). The age of the younger caldera subsidence is unknown. The uneven caldera floor is covered by glacier ice up to about 600 m depth (in 2011; Lachowycz et al. 2015) but has been shrinking over the last decades (Rivera and Bown 2013). Lithofacies and geochemical compositions of the caldera-wall rocks have been investigated by Gilbert et al. (1996), Murphy (1996) and Lachowycz et al. (2015). There is no evidence that caldera subsidence was associated with a voluminous explosive event (Gilbert et al. 1996) but lava domes straddle the southern to eastern semicircular margin of the caldera, their ascent likely guided by caldera ring-fissures (Naranjo et al. 1993). The only large explosive event known from Sollipulli is the Plinian eruption of the trachydacitic Alpehué tephra (Naranjo et al. 1993) which has been dated as 2938 ± 110 cal yr BP (Lachowycz et al. 2015). The source vent of this eruption, the 1 km diameter, 150–200 m deep Alpehué crater lies on the southwest rim of Sollipulli caldera. The most recent explosive activity on the upper northeast flank of Sollipulli emplaced the Chufquén Unit of basaltic-andesitic scoria cones and lavas at 633 ± 87 cal yr BP (Naranjo et al. 1993; Lachowycz et al. 2015).

The Alpehué eruption generated well-sorted pumice fallout dispersed towards the northeast and pyroclastic flows that partly filled valleys to the northwest, southwest and southeast with unwelded, massive ignimbrite that became subsequently partly covered by lahar deposits. Pyroclastic flow deposits also occur within the Alpehué crater where

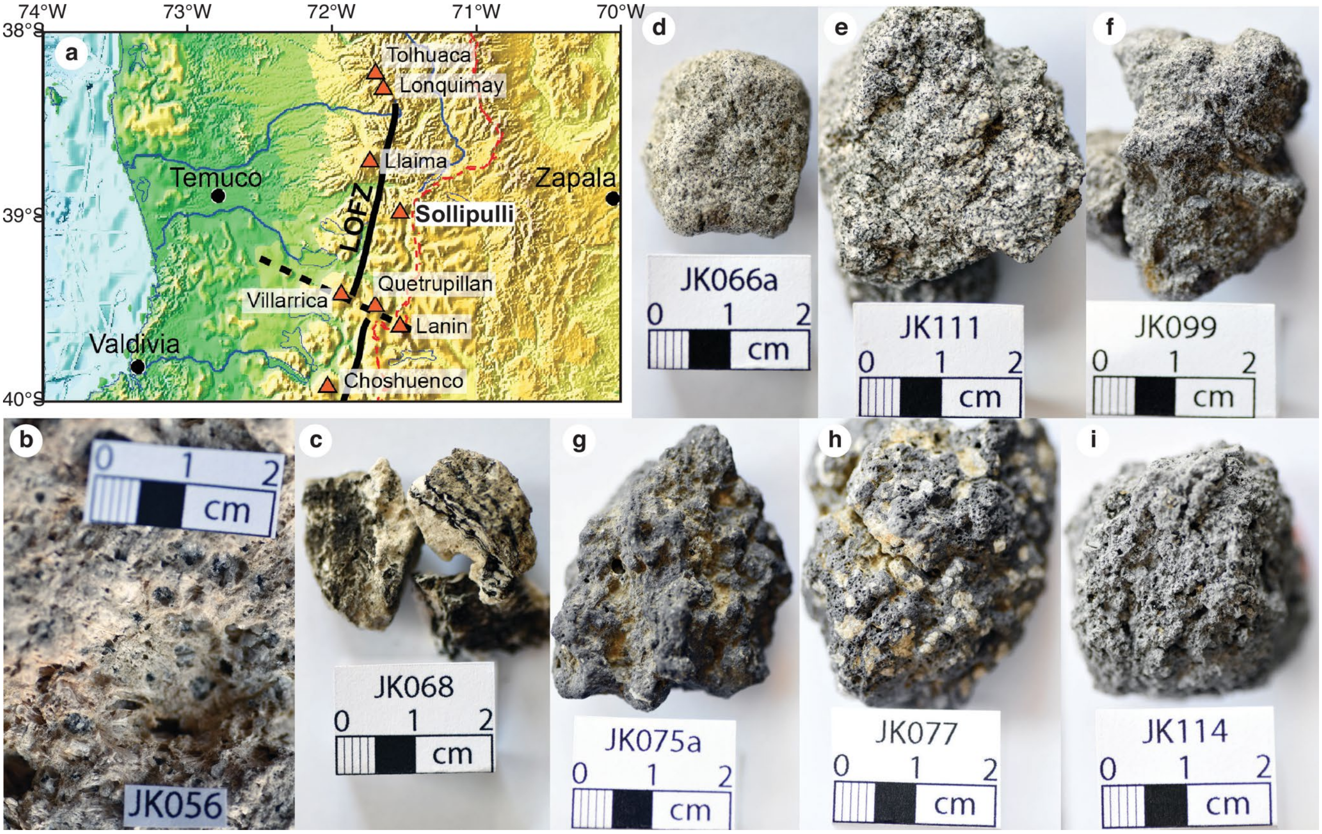

Fig. 1 (a) Topographic map of part of the Central Southern Volcanic Zone. Volcanoes Lonquimay, Llaima and Villarrica mark the volcanic front while Sollipulli (like Lanin) lies behind the front. LOFZ is the Liquiñe-Ofqui fault zone (bold black line) which is offset between Villarrica and Quetrupillan volcanoes (black dashed line). Red dashed line is Chile-Argentine border. Topography is based on a dataset of the Shuttle Radar Topography Mission (Farr et al. 2007). (b to i) Photographs of hand specimen of the samples indicated

they range from unwelded through moderately to densely welded (Gilbert et al. 1996). Naranjo et al. (1993) constrained the volume of the fallout to 7.5 km^3 and estimated the ignimbrite volume as 0.4 km^3, giving a total tephra volume of ~ 8 km^3.

Field work

We have studied the Alpehué fallout in outcrops up to 70 km distance from Sollipulli to the northeast and east, and the ignimbrite in outcrops northwest to west of Sollipulli. The lapilli fallout is vaguely stratified into five units by vertical grain-size changes and lithic-rich horizons but has no sharp layer boundaries except a thin well-stratified basal layer (photograph in supplement S1). The fallout contains two horizons rich in matrix ash: a gray crystal-rich ash horizon in the lower part and a brown fine-ash horizon in the upper part which occurs locally as two horizons ~ 10 cm apart and contains accretionary lapilli while pumice lapilli are coated with brown fine ash. The massive, poorly sorted, unwelded ignimbrite locally comprises up to 7 flow units (photograph in supplement S1) composed of gray ash with two exceptions: flow units IV and V have brown fine matrix ash. We observed thin (upwind) fallout deposits below and above the ignimbrite west and south of Sollipulli. There is no vertical compositional variation in the Alpehué tephra that would facilitate stratigraphic correlations but we interpret fallouts bracketing the ignimbrite and the occurrence of the gray and brown ash horizons in the fallout, which are probably co-ignimbrite ash, to reflect roughly synchronous Plinian and pyroclastic-flow activity.

In the field we identified and sampled the following lithologic components of the Alpehué Tephra (sample list in supplement S1):

(1) The main pumice is light gray and beige, crystal-rich and highly vesicular with vesicles ranging from microns to centimeters in size and with dominant feldspar and minor ferromagnesian phenocrysts (Fig. 1b).
(2) Banded pumice clasts are composed of viscously mingled zones differing in color due to either compositional or textural differences (Fig. 1c).

(3) Glomerocrystic clasts are crystal-rich fragments with abundant intergrown crystal clots and mostly highly vesicular interstitial glass (Fig. 1d-f) that occur with different modal compositions and crystal sizes.
(4) Dark gray, poorly to moderately vesicular, crenulate and knobbly lava clasts range from entirely microcrystalline to highly phyric (Fig. 1g-i). We interpret their shape as the result of quenching of fluid mafic magma entrained in cooler dacitic magma and hence consider them as a mafic juvenile component. The knobbly lava clasts are very similar to mafic enclaves described from lavas and plutons (e.g., Chapman 1962; Wiebe 1973; Coombs et al. 2002) but also from other tephras (e.g., Seaman and Chapman 2008; Rooyakkers et al. 2018).
(5) Medium to very coarse crystal ash, dominated by large feldspar crystals, forms a significant minor grain-size population in the fallout.
(6) Black dense angular obsidian fragments.
(7) Lithic fragments comprise volcanic rocks (weathered mafic lava fragments and scoria clasts), sedimentary rocks (schist and sandstone fragments), and dense plutonic rock fragments.

In the following we focus on the investigation of clast types 1 to 4.

The main pumice clasts are macroscopically very similar. Clast types 2–4 form a minor component in the tephra but are easily found at each outcrop and at each level in the tephra. We collected quite a number of such clasts from fallout and ignimbrite and within the banded pumice, glomerocrystic and knobbly lava clast collections we identified subgroups based on macroscopic petrographic features. We then chose clasts considered representative of the subgroups for detailed analyses. The total variability of types 2–4 clasts in the Alpehué Tephra is certainly greater than represented by our analyzed samples. Glomerocrystic and knobbly lava clasts occur (partially) mantled by main pumice as well as free clasts. Free glomerocrystic clasts probably formed by fragmentation of larger blocks during explosive eruption and their low strength facilitated rounding during transport (Fig. 1d-f). Free knobbly lava clasts often have at least one fracture surface also formed during explosive eruption; the quenched surfaces may have been breaking points where mantling pumice easily spalled off.

Analytical methods

Bulk-rock X-ray fluorescence analyses of finely ground sample powders were performed with the Pananalytical automatic wavelength-dispersive Spectrometer Magix-PRO at the University of Hamburg. Standard deviations for international reference standards are less than 0.5% for most major elements and < 10% for all measured trace elements. Further trace element concentrations were measured by Inductively Coupled Plasma-Mass Spectrometry using the Agilent 7500cs instrument at the Institute of Geosciences at the University of Kiel following the analytical procedures of Garbe-Schönberg (1993). Average precision and accuracy are below 10% for most elements based on replicate analyses of synthetic and natural standards. Glass and mineral compositions were analyzed in polished thin sections with a JEOL JXA 8200 wavelength dispersive electron microprobe (EMP) at GEOMAR in Kiel using 15 kV accelerating voltage and measuring programs calibrated with international natural and synthetic standards in which beam current and beam focus were adjusted for each phase following Kutterolf et al. (2011). The deviations are < 0.5% for major elements and < 3% for minor elements. The bulk-rock, glass and mineral analytical data are compiled in Tables S2 and S3.

Bulk-rock geochemical compositions

Murphy (1996) investigated the magmatic evolution of Sollipulli and we use his bulk-rock geochemical data on the pre-Alpehué Aleta del Tiburòn (AT) and circum-caldera (CC) units to complement our Alpehué data. The Alpehué magmatic components include basaltic to basaltic-andesitic knobbly lava clasts, glomerocrystic clasts covering the wide range from basalt to trachyandesite-trachyte bulk compositions, the trachydacitic main pumice (65 to 69 wt% SiO_2) and two rhyolitic obsidian clasts (O1, O2), which all form a common liquid line of descent together with the other Sollipulli rocks (Fig. 2a). This trend is also shared by dioritic and granodioritic plutonic xenoliths which differ from glomerocrystic clasts by being holocrystalline and containing evidence of sub-solidus reactions such as chloritization and feldspar exsolution textures. The Sollipulli compositions define a linear increase in K_2O with SiO_2 (Fig. 2b). Linear correlations are also observed between other relatively incompatible elements such as Rb and K_2O, and Ba and Zr (Fig. 3) although Rb became more incompatible than K_2O in the trachydacite while Ba became more compatible than Zr.

This suggests fractional crystallization as the main process of differentiation at Sollipulli (cf. Murphy 1996). Selected SiO_2 and MgO variation diagrams (Figs. S4 and S5 in the supplement) show the variations expected from early olivine, calcic plagioclase and clinopyroxene fractionation as well as significant fractionation of Fe-Ti oxide at MgO < 3–4 wt%, and of sodic plagioclase and apatite at SiO_2 > 60–65 wt%. Figure 4a illustrates the compositional

Fig. 2 (a) Bulk-rock total alkalis versus SiO_2 contents with subdivision after Le Maitre et al. (1989). Data for older Sollipulli volcanic deposits from Murphy (1996). (b) Linear increase in K_2O with silica up to the glass composition of the main pumice and obsidian fragments O1 and O2. Melt inclusions in orthopyroxene in banded pumice JK068 lie off that trend. Bars at top of graph: amphibole phenocrysts are absent in the most mafic basaltic and glomerocrystic clasts (left gray) as well as in the trachydacite (right gray) but abound in intermediate compositions (orange). (c) Minimum total crystallinity of samples calculated from the concentration ratio of K_2O in bulk-rock and glass. High crystallinities of knobbly lava samples and mafic glomerocrystic clast JK003 are strongly influenced by matrix crystallization

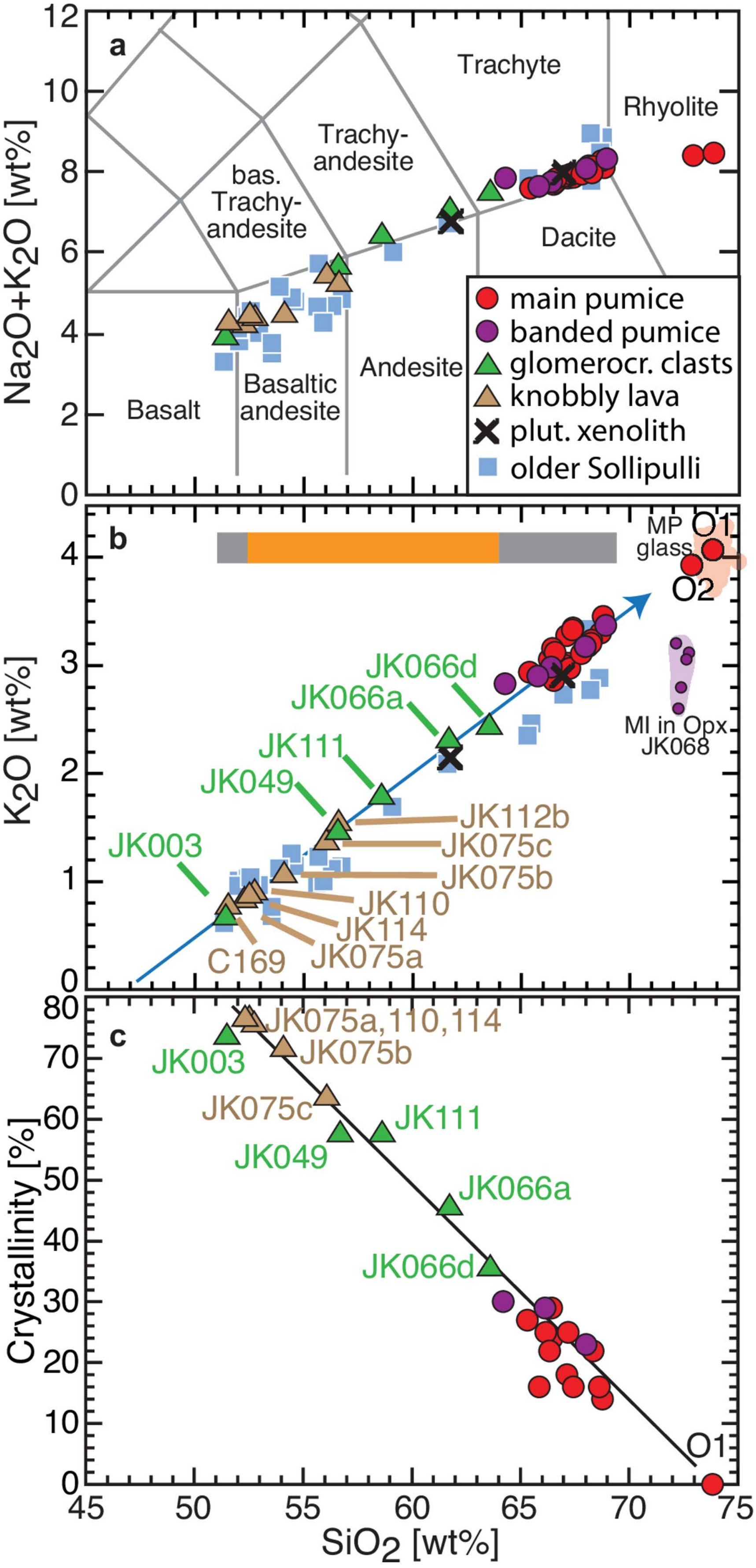

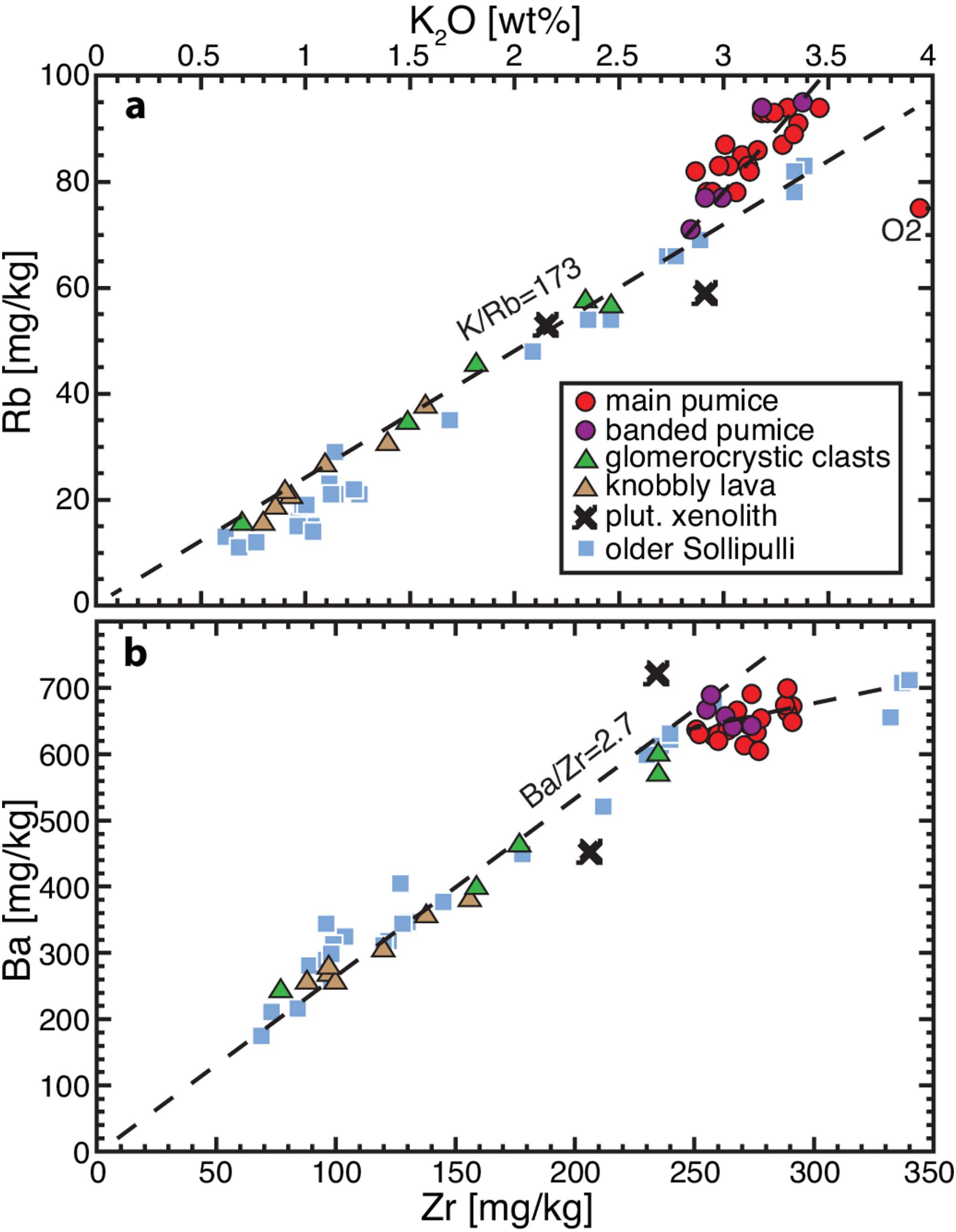

Fig. 3 Mostly linear variations in (a) Rb versus K$_2$O and (b) Ba versus Zr bulk-rock concentrations. In the main-pumice trachydacite Rb is less, and Ba more compatible with respect to K$_2$O and Zr. Note how obsidian fragment O2 deviates from the main trend

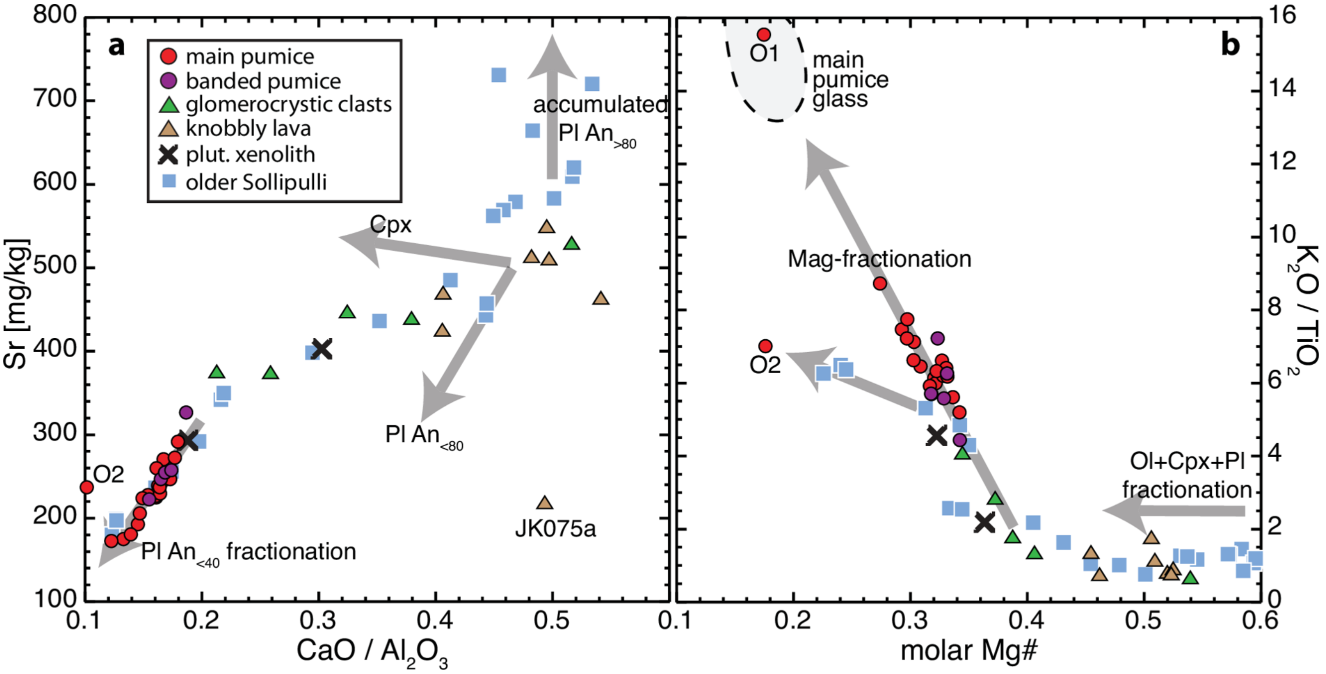

Fig. 4 (a) Bulk-rock Sr versus CaO/Al_2O_3 (by weight) diagram with gray arrows illustrating the effects of plagioclase accumulation in some mafic Sollipulli rocks, combined plagioclase-clinopyroxene fractionation across the intermediate range, and plagioclase-dominated fractionation in the trachydacite. (b) K_2O/TiO_2 (by weight) versus molar Mg-number (Mg#) diagram illustrating the change from earlier olivine (Ol), plagioclase (Pl) and clinopyroxene (Cpx) fractionation to strong titanomagnetite (Mag) fractionation in the evolved rocks with steep TiO_2 depletion leading to main-pumice glass and obsidian O1 compositions while less TiO_2 depletion formed older Sollipulli trachydacites and obsidian O2

variations due to changing plagioclase-clinopyroxene ratios and plagioclase An-contents in the fractionated assemblage, and suggests accumulated plagioclase in some of the older mafic Sollipulli rocks. Similarly, Fig. 4b shows that titanomagnetite fractionation at Mg#<0.4 evolved differently in the Alpehué trachydacite compared to older Sollipulli trachydacites.

The two analyzed obsidian fragments from the Alpehué tephra reach the high SiO_2 contents of matrix-glass (Fig. 2b) but only O1 has the same glass composition as the Alpehué trachydacite (Fig. 4b, S4a, d) while O2 deviates to lower Al_2O_3 and higher P_2O_5, TiO_2, and FeO (Figs. S4a, d, S5a, b), has higher K/Rb = 218 (Fig. 3a) and low K_2O/TiO_2 comparable to older Sollipulli trachydacites (Fig. 4b). Thus obsidian clast O1 represents a precursory extrusion from the Alpehué trachydacite reservoir and obsidian clast O2 is a xenolith probably ripped off one of the older evolved domes exposed in the Alpehué crater (Gilbert et al. 1996).

Petrography

The high vesicularity of most samples studied here makes it difficult to visually estimate vesicle-free crystal contents which we therefore calculate from the ratio of K_2O concentrations in matrix glass and bulk-rock according to Rayleigh fractional crystallization. The assumption of perfect incompatibility for K_2O yields minimum crystallinities (Fig. 2c). The main petrographic features are summarized in supplement Table S6.

Main pumice

The phenocryst contents of 14–29% of the trachydacitic pumice mainly include large compositionally zoned plagioclase crystals (≤3 mm) mostly forming even larger aggregates (≤6 mm) of intergrown crystals (Fig. 1b), and minor smaller plagioclase crystals with little or no visible zonation. The compositionally zoned plagioclase crystals typically consist of a partially resorbed core (RC) with melt inclusions, an inner thinly stratified mantle zone (IZ) followed by a resorbed zone (R) rich in melt inclusions, and an outer stratified zone (OZ) (Fig. 5). In all main pumice thin sections, we observed in-situ fragmented larger plagioclase crystals and smaller plagioclase fragments of angular shapes and discordantly cut zonation patterns. The second abundant phenocryst phase is euhedral orthopyroxene up to 1.6 mm long. Minor phases are mostly subhedral to anhedral clinopyroxene, titano-magnetite and subordinate ilmenite as well as accessory apatite. All the minor mineral phases can be found intergrown with plagioclase and with each other. In just 2 of the 12 main-pumice thin sections studied we

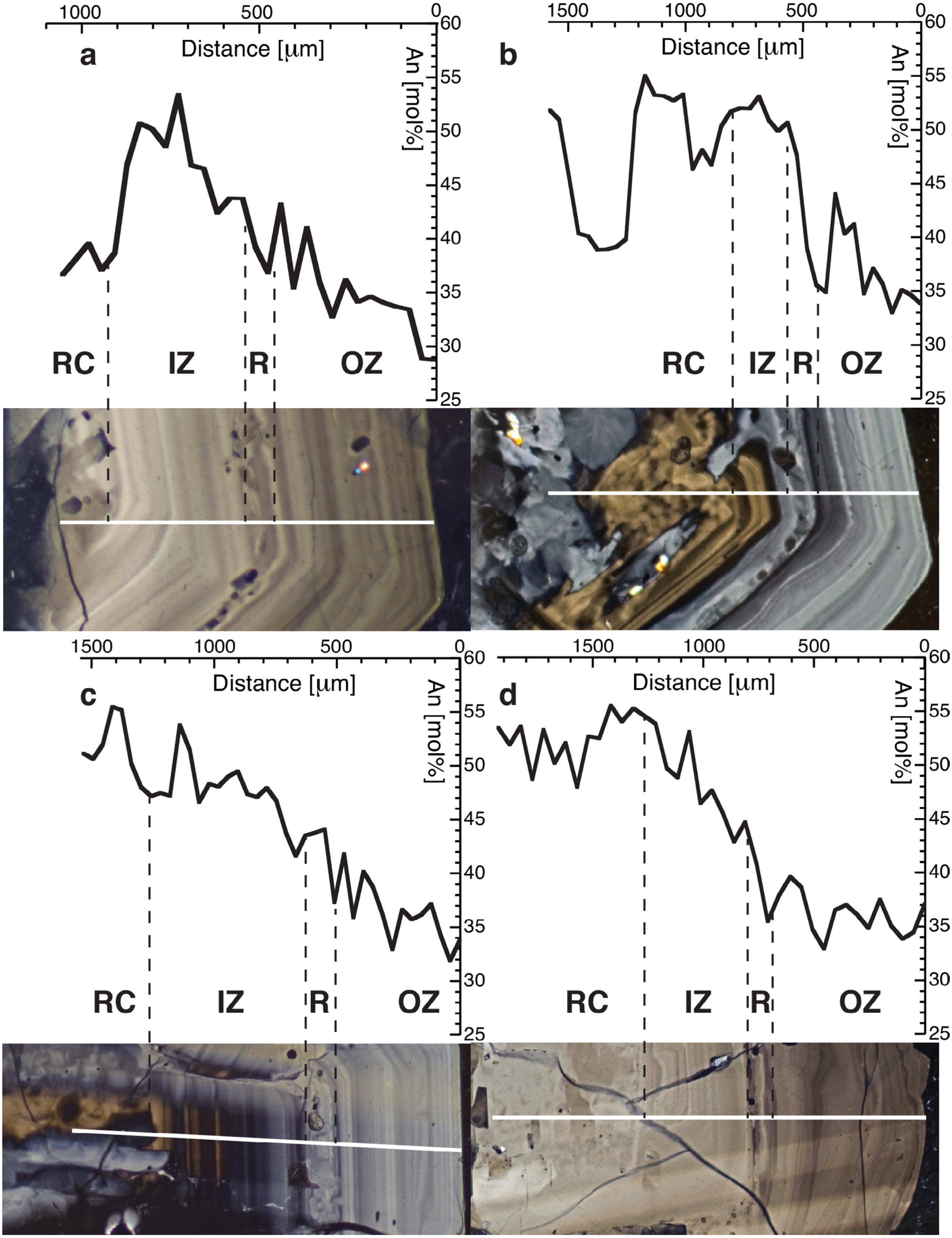

Fig. 5 Example compositional profiles (An content versus distance from rim) through zoned plagioclase phenocrysts of the main pumice. Thin section photographs with crossed polarizers. We distinguish patchy resorbed cores (RC), an inner compositionally stratified zone (IZ), a resorption interval (R) with melt inclusions, and an outer stratified zone (OZ). Close inspection of the photographs reveals minor unconformities also within IZ and OZ

observed one amphibole each: a euhedral lath 180 µm long (sample JK057a) and an anhedral splinter about 500 µm long (sample JK055), both isolated in matrix glass and without resorption. All main pumice clasts are highly vesicular, some show textures of intense viscous shearing with strongly elongated vesicles, and large crystals or crystal clots that are often mantled by a vesicle corona suggesting their surface favored bubble nucleation. The clear to light brown matrix glass contains very few tiny Fe-Ti oxide and minor pyroxene microlites.

Glomerocrystic clasts

All investigated samples of this group differ petrographically and are thus described separately. They all contain highly inflated glass matrix so that most crystals/crystal clots do not touch each other. The calculated vesicle-free crystallinities of 36–58 vol% (Fig. 2c) indicate that these samples represent magmatic crystal mush before vesiculation (according to Marsh (1989) crystal mush contains 25 to 55% crystals). The most extremely inflated example (JK107) is a fine-grained (100–300 µm) glomerocrystic clast of plagioclase, partly disintegrated clinopyroxene and fresh orthopyroxene dispersed by almost reticulitic foam (Fig. 6a). The inflated glomerocrystic clasts differ from the main pumice in several aspects but most important is the presence of abundant amphibole in all but the most mafic sample.

The most mafic glomerocrystic clast JK003 (cf. Figure 1f) contains plagioclase, clinopyroxene, olivine and magnetite which often form intergrown clots in which plagioclase is ~800 µm long. This glomerocrystic clast contains no amphibole and no orthopyroxene. There are also separate plagioclase crystals up to 2800 µm long with sieve-textured, strongly resorbed core and minor zonation in the rims. The matrix ranges from light-brown highly and coarsely vesicular glass to glass with much smaller vesicles that contains abundant lath-shaped plagioclase and clinopyroxene microcrysts (about 150 µm in size) which locally form radial quench-crystallization textures of up to 300 µm long needles. The total calculated crystallinity of 74% (Fig. 2c) is thus partly due to such quench-crystallization.

In glomerocrystic clast JK111 (Fig. 1e) of intermediate bulk composition the major phenocryst phases are plagioclase, amphibole, clinopyroxene and orthopyroxene (in order of abundance) as well as minor magnetite and apatite, which all occur as euhedral individual crystals but also intergrown with each other. Plagioclase laths are up to 1200 µm long and only rarely zoned. Most amphibole laths are 400–600 µm long but some up to 6 mm long crystals occur. Almost all long crystals are fractured in situ by longitudinal extension (Fig. 6b). While most orthopyroxene crystals are small (~100 µm) and euhedral, particularly the larger clinopyroxene crystals have lost part of their euhedral shape and have been partially replaced by amphibole (cf. Figure 6c). The pumiceous clear glass matrix has no microlites so that the calculated crystallinity of 58% (Fig. 2c) is due to phenocrysts.

Glomerocrystic clast JK049 has similar bulk and modal compositions as JK111 and also similar vesicle-free phenocryst content of 58% (microlites are very rare in the clear glass). Phenocrysts reach ~600 µm in size but there are also abundant small (40–200 µm) angular anhedral crystal fragments. Most crystal clots are formed by plagioclase, clinopyroxene and magnetite and rarely contain olivine (in one case overgrown by orthopyroxene). The clinopyroxene crystals in these clots as well as larger free clinopyroxene crystals are partly replaced by amphibole (Fig. 6c). Amphibole is rarely intergrown with plagioclase but mostly forms separate subhedral crystals. A few large plagioclase crystals have rounded sieve-textured cores mantled by fresh euhedral rims (Fig. 7a).

The evolved glomerocrystic clasts JK066a (Fig. 1d) and JK066d contain highly vesicular clear glass without microlites. Average crystal concentrations are 46% and 36%, respectively, but vary between schlieren-like regions in which elongated crystals are mostly flow-aligned. The common phenocryst assemblage is plagioclase, amphibole, orthopyroxene, magnetite and rare apatite. Trachyandesitic JK066a contains clinopyroxene or olivine in rare crystal clots with plagioclase and magnetite. Plagioclase laths are about 400 µm long while amphibole laths and orthopyroxene crystals are around 200 µm and occur intergrown with, or included in, plagioclase. Trachytic JK066a contains brown pleochroic amphibole and some dark-brown blocky biotite crystals of comparable size. Biotite and mafic crystal clots are not found in sample JK066d, which also differs by a much lower fraction of amphibole and by crystal sizes being limited to around 200 µm.

Knobbly lava

The nine petrographically investigated knobbly lava clasts can be divided into three types of three clasts each. Type 1 is poorly vesicular (Fig. 1g), microcrystalline with very few phenocrysts of mostly un-zoned plagioclase, olivine and minor clinopyroxene. Some rounded, sieve-textured large plagioclase crystals are present in all three samples, some intergrown with orthopyroxene and magnetite (Fig. 7b). The microcrystalline matrix has a diktytaxitic texture of randomly oriented plagioclase laths (50–170 µm in JK110, 200–300 µm in JK075a), amphibole needles, opaque oxide, and minor olivine with interstitial vesicular glass which is best visible along vesicle margins (Fig. 6d). The calculated

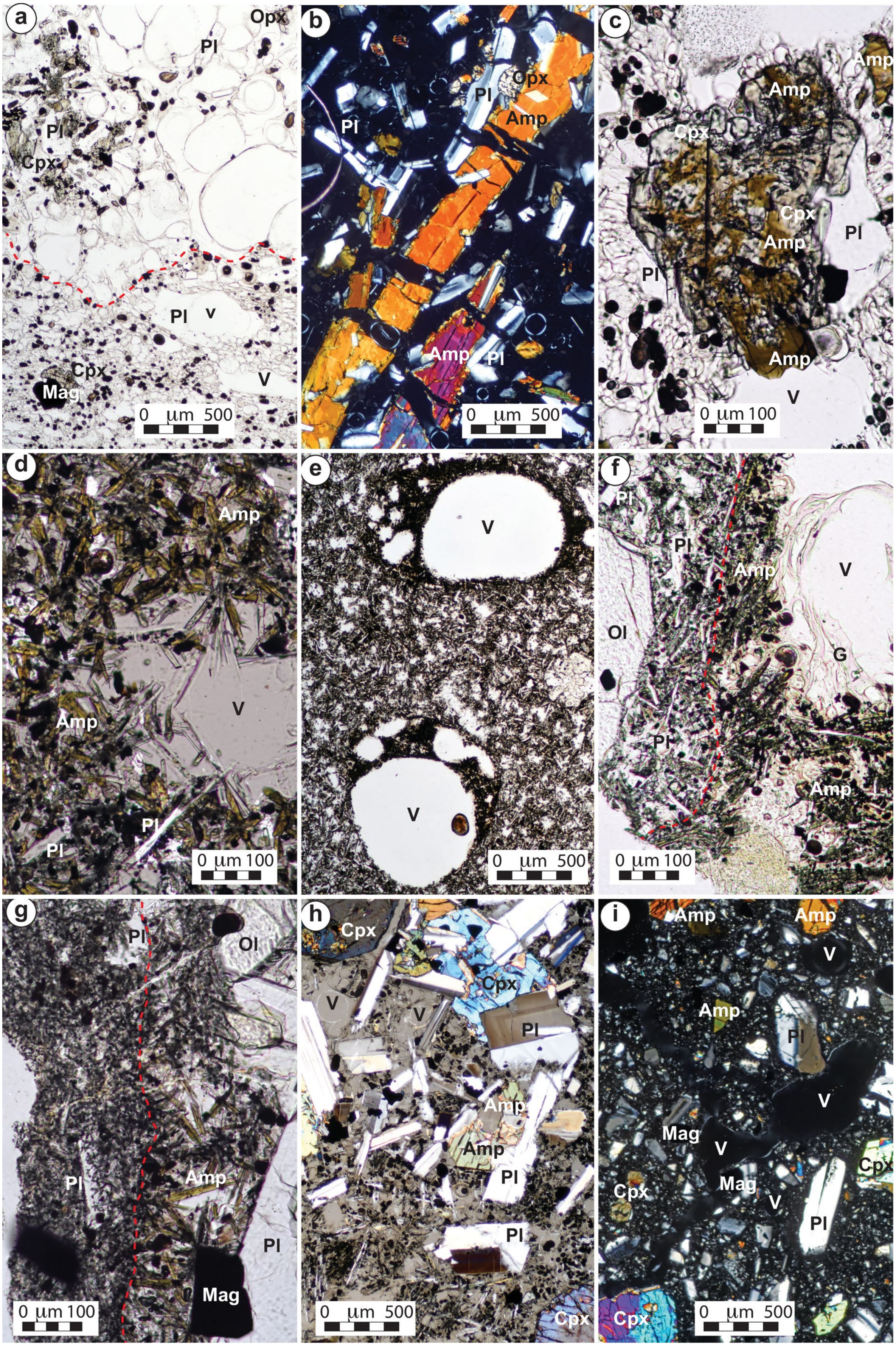
a
Opx
Pl
Pl
Cpx
Pl
V
Cpx
Mag
V
0 µm 500
b
Opx
Pl
Pl
Amp
Amp
Pl
0 µm 500
c
Amp
Amp
Cpx
Cpx
Pl
Amp
Pl
Amp
V
0 µm 100
d
Amp
V
Amp
Pl
Pl
0 µm 100
e
V
V
0 µm 500
f
Pl
Pl
Amp
V
Ol
G
Pl
Amp
0 µm 100
g
Pl
Ol
Pl
Amp
Pl
Mag
0 µm 100
h
Cpx
Cpx
V
V
Pl
Amp
Amp
Pl
Pl
Cpx
0 µm 500
i
Amp
Amp
V
Amp
Pl
V
Mag
V
Cpx
Mag
V
Cpx
Pl
Cpx
0 µm 500

◀ **Fig. 6** Photomicrographs of various Alpehué samples. (a) Extremely inflated glomerocrystic clast (top half of image) in contact (red dashed line) with main pumice (lower half). JK107, transmitted light. (b) Glomerocrystic clast JK111 with large and long amphibole crystals. Long amphibole and plagioclase laths were practically all fractured in situ. Some fractures are filled by dense glass, others by vesicular glass, and some by vesicles filling almost the entire fracture. Crossed polarizers. (c) Amphibole partly replacing clinopyroxene in glomerocrystic clast JK049. Transmitted light. (d) Amphibole and plagioclase needles dominate the matrix of type-1 knobbly lava JK110. Transmitted light. (e) Large round vesicles in type-2 knobbly lava C169, with matrix rims containing further vesicles. Transmitted light. (f) The quenched amphibole, plagioclase and glass matrix (right) of the vesicle rims in (e) in contact (red dashed line) with the plagioclase-dominated lava matrix (left). Transmitted light. (g) Contact (red dashed line) between fine-grained lava matrix (left) and coarser, amphibole-rich glomerocrystic region matrix (right) in type-3 knobbly lava JK075c. Transmitted light. Note the yellow-greenish colors that distinguish amphibole-bearing (right) from amphibole-free (left) matrix in (f) and (g). (h) Glomerocrystic fragment in an apparent state of disintegration in type-3 knobbly lava JK075b. Note partly subophitic texture of some crystal clots with clinopyroxene between plagioclase laths. Darker, stippled regions (bottom and lower right) are regions of lava matrix mingled with the glomerocrystic region which has long plagioclase and amphibole needles in its matrix. Half-crossed polarizers. (i) Knobbly lava sample JK114 has a seriate texture in which crystal mush-derived minerals and abundant angular fragments thereof are dispersed in the basaltic matrix with irregularly shaped vesicles. Crossed polarizers. Abbreviations: Amp = amphibole, Cpx = clinopyroxene, Mag = titanomagnetite, Ol = olivine, Opx = orthopyroxene, Pl = plagioclase, V = vesicle, G = glass

crystallinities of 76–77% dominantly reflect microlite crystallization.

Type 2 knobbly lavas contain a significant fraction of large phenocrysts of plagioclase (up to 3.6 mm) and olivine (≤2.8 mm), some forming large densely intergrown glomerocrysts up to 8 mm in diameter (Fig. 1h) and are practically unzoned (Fig. 7c). Rare zoned plagioclase crystals show no resorption (as in type 1 samples) but are classified as xenocrysts because they are intergrown with orthopyroxene (as in trachydacite). Plagioclase, clinopyroxene and magnetite dominate over olivine in the microcrystalline matrix while amphibole is absent; clear glass with small irregular vesicles is sometimes preserved in interstitial pores (Fig. 6e, f). The calculated crystallinity of 77% describes the combination of phenocryst and matrix crystallinity. Type 2 samples are poorly vesicular with just few round vesicles in the matrix. However, there are also larger vesicles and vesicle-clusters with dark matrix rims (Fig. 6e) composed of quench-needles of plagioclase and amphibole with highly vesicular clear glass in irregular pores (Fig. 6f), clearly distinct from the surrounding amphibole-free type-2 matrix.

Type 3 knobbly lava clasts contain mingled "glomerocrystic regions" and "lava regions". The thin section of JK075b is largely occupied by a glomerocrystic region of poorly or unzoned plagioclase laths, clinopyroxene, amphibole, olivine, orthopyroxene, and magnetite crystals (< 1600 μm in size). While mostly plagioclase laths form a diktytaxitic texture, crystal clots of plagioclase-clinopyroxene-(± olivine) have a subophitic texture (Fig. 6h). Clinopyroxene is partly replaced by amphibole. The interstitial matrix in the glomerocrystic region consists of clear highly vesicular glass with about 200 μm long skeletal needles of plagioclase and amphibole. The surrounding and penetrating lava-like microcrystal-rich matrix (Fig. 6h) has clear vesicular glass but is much more crystallized, plagioclase laths are much smaller (50–100 μm) and by far dominate the matrix composition. The phenocrysts in this lava region are the same as in the glomerocrystic region, with the same intergrowths, and many surrounded by microlite-poor vesicular glass as in the glomerocrystic region; they therefore seem to have been inherited from the partly disintegrated crystal mush rather than having crystallized in place.

Such an apparent state of disintegration is also seen in thin section JK075c but here the glomerocrystic region is composed of plagioclase, clinopyroxene and olivine crystals as well as some larger, rounded plagioclase crystals with intense fingerprint resorption mantled by a thin overgrowth rim (fingerprint texture is a fine-grained sort of sieve texture). There are no amphibole phenocrysts but the matrix of the glomerocrystic region contains skeletal 200–300 μm long needles of amphibole and plagioclase in highly vesicular clear glass (Fig. 6g). The moderately vesicular matrix of the surrounding and pervading lava region is almost cryptocrystalline (< 25 μm) and vastly dominated by plagioclase, with some larger plagioclase laths (50–100 μm) (Fig. 6g). The phenocrysts are poorly zoned plagioclase, clinopyroxene, olivine and magnetite, which form intergrown clots, as well as amphibole, which is mostly solitary but also occurs intergrown with plagioclase and partly surrounds some clinopyroxene. Several large plagioclase crystals intergrown with clinopyroxene (and rarely with orthopyroxene) have intensely fingerprint-resorbed interiors. While most phenocryst phases in the lava region could potentially be inherited from the disintegrating glomerocrystic crystal mush, the amphibole crystals and phases intergrown with them may be original phenocrysts but could also be inherited from amphibole-bearing crystal mush as in JK075b. Calculated bulk crystallinities of 64–72% in type-3 samples (Fig. 2c) are difficult to interpret because glass analyses are dominantly from the glomerocrystic regions while bulk-rock composition includes the lava regions as well.

Sample JK114 (Fig. 1i) does not have the two distinct regions of the other samples, its microcrystalline matrix (laths of plagioclase, amphibole, rare olivine) is rather uniform and moderately vesicular with dispersed smaller, oval and some large irregularly shaped vesicles (Fig. 6i). The phenocryst population consists of plagioclase, olivine, clinopyroxene, amphibole, magnetite and accessory apatite, and the calculated crystallinity of 77% is a combination of phenocryst and microlite crystallization. Isolated, subhedral to euhedral phenocrysts about 600–1200 µm in size are less abundant than mineral clots up to 2.5 mm diameter that range from dense intergrowth to accumulations with significant interstitial space, which in rare cases is filled by clear vesicular glass. Plagioclase-olivine clots abound, followed by those of plagioclase with large clinopyroxene (that is often partly resorbed and replaced by amphibole), plagioclase-clinopyroxene-olivine, and plagioclase-olivine-amphibole. In contrast to clinopyroxene, olivine in contact with amphibole shows no reaction. Most large blocky plagioclase crystals but also a fraction of the smaller lath-shaped crystals, are internally resorbed, particularly those intergrown with only clinopyroxene. There is a second, smaller population (about 200 µm) of anhedral angular fragments and few euhedral crystals of mainly plagioclase but also of the ferromagnesian phases (Fig. 6i). We associate sample JK114 with the third group of knobbly lavas because the abundance and diversity of the crystal aggregates suggests they may have been accumulated from various crystal mush sources (with and without amphibole or olivine).

Banded pumice

In some clasts, irregular speckles (JK057c) and long bands (JK057b) of darker regions are more finely vesicular and have more microlites then the surrounding lighter pumiceous regions but there is no mineralogical difference between them; they have the typical modal composition of the main pumice. This is also the case in sample JK124 where darker zones of finer vesicles and rich in small angular crystal fragments represent shear zones between lighter zones of coarser vesicles. Sheared sample JK112a has darker zones in which some amphibole, even included in plagioclase, can be found and which thus differ compositionally from the main pumice. In banded pumice JK038 larger phenocrysts (main-pumice assemblage) seem to be excluded from darker shear zones and the sample contains abundant small crystal fragments. A few small euhedral amphibole crystals (about 50 µm) occur in a darker zone. All the sheared samples contain a few xenoliths (plutonic and mafic lava; 0.5–3.5 mm). Banded pumice JK068 (Fig. 1c) is compositionally the most diverse. Schlieren-like dark, intermediate and light zones with highly variable microlite (50–100 µm) contents in clear glass matrix, host a range of phenocrysts from intensely zoned large plagioclase with orthopyroxene (as in the main pumice), through plagioclase crystals with intense internal fingerprint resorption and clinopyroxene-plagioclase aggregates to large olivine crystals and olivine-plagioclase aggregates with adhering brown glass (as found in mafic glomerocrystic and knobbly lava samples).

Glass geochemical compositions

With very few exceptions, the matrix glass compositions of the main pumice samples are very uniform with mean $SiO_2 = 73.9 \pm 0.3$ wt% (Fig. 8). Melt inclusions, mostly in plagioclase but also in orthopyroxene and magnetite, overlap with the matrix glass compositions but extend to slightly higher MgO concentrations (Fig. 8b, d). Matrix glass in banded pumice samples mostly has the same composition as in main pumice supporting that banding in these samples is formed by textural rather than compositional differences. In contrast, compositionally banded sample JK068 contains three matrix glass populations (Fig. 8a). The high-silica population overlapping with white-pumice matrix is the common glass composition in the sample, the low-silica population is interstitial brown glass in olivine-plagioclase crystal clots, and the intermediate population is glass on the outside of such clots, probably a result of mixing. One orthopyroxene of JK068 contains melt inclusions with relatively low K_2O but high MgO compared to main pumice glass (MI in Opx, Fig. 8b, d); this is a xenocryst possibly derived from older, less potassic Sollipulli trachydacite (Fig. 2b).

The glomerocrystic samples distribute into three glass-compositional groups. The most mafic glomerocrystic clast JK003 has the least evolved matrix glass (around 65.8 wt% SiO_2; Fig. 8a, c). Matrix glasses of glomerocrystic samples JK049 and JK066d form a population between 72.3 and 73.7 wt% SiO_2, and JK066a and JK111 a population at 74.4–75.5 wt% SiO_2 (Fig. 8b). Melt inclusions in glomerocrystic clast JK049 are less evolved (69.8–72.1 wt%) than the respective matrix glass with no systematic compositional difference between inclusions in plagioclase, orthopyroxene, magnetite or amphibole.

Matrix glasses in the phenocryst-poor microcrystalline type 1 knobbly lava samples (JK110, JK075a) are equally highly evolved as in main pumice and evolved glomerocrystic clasts (Fig. 8b) mainly as a result of microlite growth (Fig. 6d). In type-2 sample C169 the only successful measurements were in high-silica interstitial glass in a large clot of zoned plagioclase and orthopyroxene, and thus represent main-pumice glass. The type 3 knobbly lava samples (JK075b, c) are mixtures between microcrystalline lava regions and glomerocrystic regions (Fig. 6h), and the very wide range in glass compositions (Fig. 8) includes more evolved compositions measured in the microcrystalline lava regions and less evolved compositions of vesicular glass in the glomerocrystic regions and adhering to crystals admixed

Fig. 7 (a) Compositional profile across a plagioclase with rounded resorbed xenocrystic core and euhedral overgrowth in glomerocrystic clast JK049. Orange arrows point at interior zones of microcrystalline clinopyroxene (?). Blue arrow points at clinopyroxene intergrown with plagioclase overgrowth that is partly replaced by amphibole. (b) Compositional profile across rounded fingerprint-resorbed moderate-An plagioclase with thin high-An overgrowth rim in type-1 knobbly lava JK110. (c) Compositional profiles across large olivine and plagioclase crystals in a crystal clot of type-2 knobbly lava C169. The olivine is practically homogeneous and the plagioclase shows only very limited chemical zonation. All microphotos in transmitted light

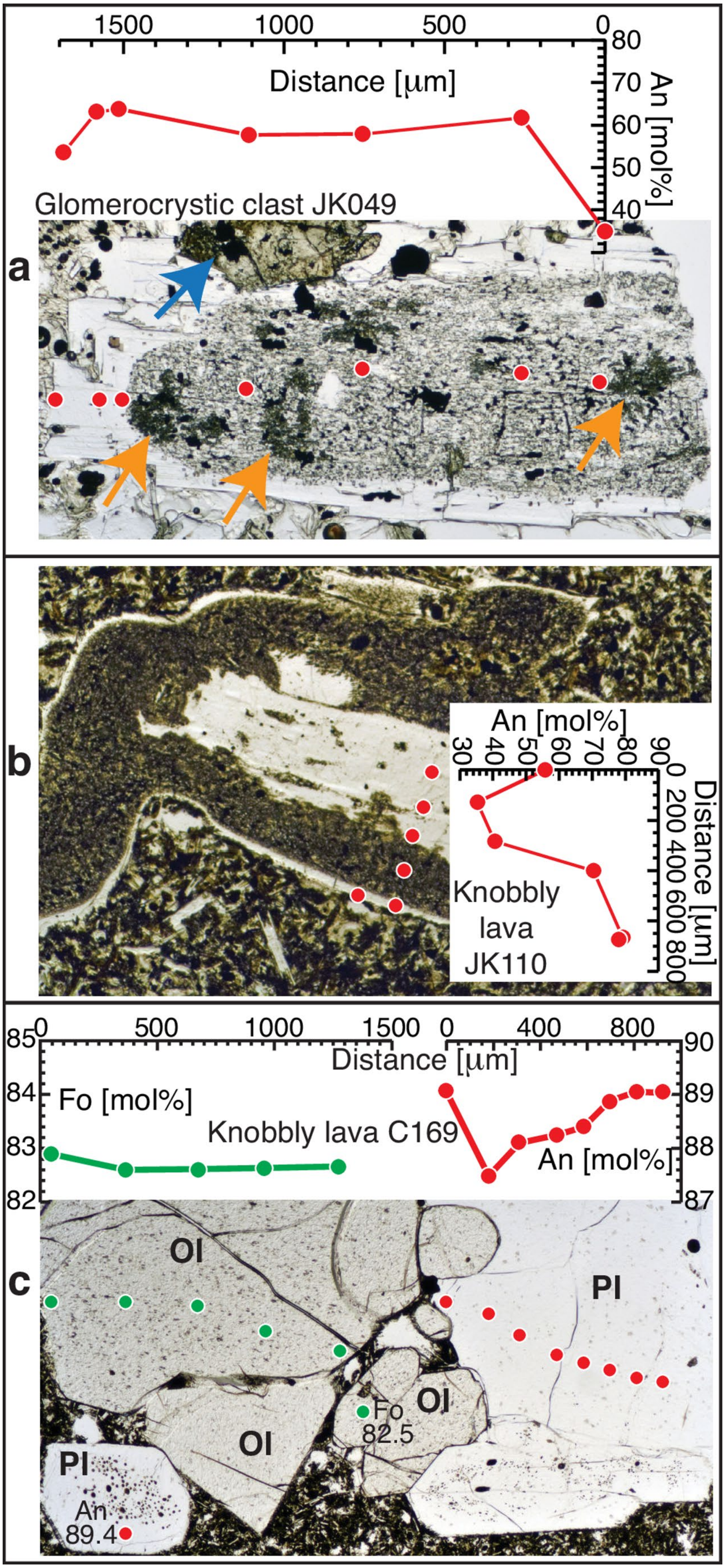

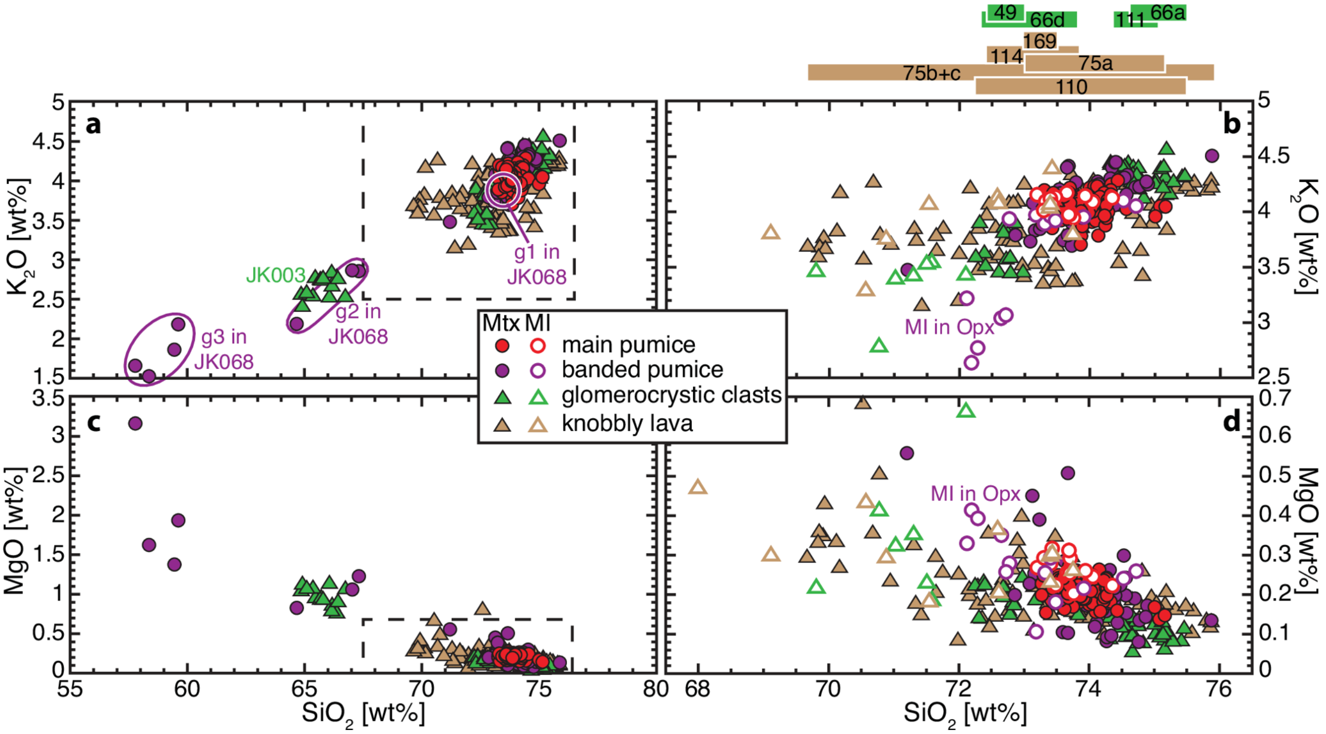

Fig. 8 (a, b) K_2O and MgO (c, d) variations over SiO_2 of matrix (Mtx) and melt-inclusion (MI) glasses. Dashed boxes in (a, c) define the enlarged areas in (b, d). g1, g2 and g3 are three glass-compositional groups found in banded pumice JK068. Except for the matrix glass of mafic glomerocrystic clast JK003 all other rocks have rhyolitic glass compositions with great overlap between melt-inclusion and matrix compositions. (b, d) Melt inclusions in an orthopyroxene (MI in Opx) in a banded pumice differ from other glasses by lower K_2O and higher MgO (see also Fig. 2b). Color-coded bars above (b) indicate the ranges of matrix-glass compositions found in the respective samples. Note that glass data for C169 is all from the large rimmed vesicles (Fig. 6e), other matrix glass could not be measured

from there into the microcrystalline lava region. The more intensely mixed type-3 sample JK114 (Fig. 6i) has relatively homogeneous interstitial glass (71–74 wt% SiO_2; Fig. 8). Melt inclusions in the knobbly lava samples large enough for analysis were only found in crystals derived either from glomerocrystic material or from main pumice, and they therefore overlap with the melt-inclusion compositions in these two rock types.

Mineral compositions

Plagioclase

Plagioclase phenocryst compositions of the main pumice form a well-defined trend of Or increasing up to 4 mol% towards lower An in the range $32 < An < 56$ mol%, a few crystal rims even reach Or > 4 mol% (Fig. 9a). Example profiles through zoned crystals (Fig. 5) show that An-contents generally, but unsteadily decrease outwards across the inner (IZ) and outer (OZ) compositionally stratified zones that mantle a resorbed core (RC) of An > 47 mol% and are separated by a resorption horizon (R) across which An content drops steeply (best developed in Fig. 5b, d). The resorbed core is a speckled zone (under crossed polarizers) associated with either low An contents (Fig. 5a, An 37–40 mol%), high An-contents (Fig. 5c, d, An 48–55 mol%), or both (Fig. 5b). Outward of the band of resorption (R) An contents remain < 45 mol%; all An concentrations > 45 mol% occur only in the inner mantle (IZ) and the core region (RC) (Fig. 9a).

Plagioclase in the glomerocrystic samples ranges across $32 < An < 80$ mol%, ignoring rare more sodic rim and matrix data, and generally follow a trend of Or enrichment towards lower An that differs from that of the main pumice. Exponential fits through the two data groups reveal that the mean difference in Or increases from 0.3 to 0.6 mol% as An content decreases from 56 to 32 mol% (Fig. 9a). Compositional ranges within single glomerocrystic clasts vary (Fig. 9c). In mafic glomerocrystic clast JK003 the plagioclase composition is generally limited to 75–79 mol% An but some outermost rim compositions have 47–53 mol% An. Plagioclase An-contents vary widely (over 30–40 mol%) and largely overlap in the intermediate glomerocrystic clasts (JK111, JK049). In JK111 core (An = 55–79 mol%) and rim (An = 33–59 mol%) compositions overlap little and unzoned plagioclase laths have a limited range of An = 42–51 mol%. In JK049 crystals are zoned over An = 70–44 mol% but outermost rims have An = 38 – 33 mol%, partly overlapping with unzoned laths of An = 53–38 mol%. Intensely fingerprint-resorbed interiors of some plagioclase crystals have An = 64–57 mol% (Fig. 7a) and some spot compositions fall on the main-pumice trend (Fig. 9a) but the majority do not. Plagioclase compositions in the two evolved glomerocrystic clasts (JK066a, d) are limited to the narrow range $32 < An < 46$ mol%.

Type 1 and 2 knobbly lavas (JK110, C169, JK125b) have the most calcic plagioclase compositions (86–91 mol% An, Fig. 9b, c) and are practically unzoned (Fig. 7c). In knobbly lava C169 the plagioclase needles in the quenched rims around larger vesicles (Fig. 6e, f) have significantly more sodic compositions (38–50 mol% An) than plagioclase in the microcrystalline lava matrix (64–73 mol% An; Fig. 9c). Plagioclase crystals in type 3 knobbly lavas show wide ranges in core and rim compositions indicative of significant zonation (JK075b, c). However, plagioclase compositions in sample JK114 are limited to the narrow interval An = 74–89 mol% clearly separated from a few overgrowth rims of An = 56–58 mol%.

Petrographic observations suggest that only the An > 80 mol% plagioclase crystals may represent equilibrium phenocrysts of the original basaltic magmas. Many, if not all, larger plagioclase crystals of lower-An compositions are xenocrysts where those of An < 50 mol% (typically partly resorbed, zoned plagioclase occasionally intergrown with orthopyroxene) lie on the main-pumice Or-An trend (Fig. 9b) and were entrained from the trachydacite magma while those of An > 50 mol% follow the glomerocrystic Or-An trend and were derived from mafic to intermediate crystal mushes. We see no evidence for entrainment of plagioclase from evolved crystal mush (such as represented by samples JK066a, d) into basalt because the few crystals of An < 50 mol% lying on the glomerocrystic trend (Fig. 9b) are needle-shaped matrix crystals grown in-situ; however, this observation may be an artifact of the limited number of samples.

Banded pumices with textural rather than compositional banding have the typical plagioclase phenocryst compositions of the main pumice (< 50 mol% An; Fig. 9b) with the same zonation patterns. An interesting exception is such a zoned crystal in sample JK112a with an overgrowth rim of 26 mol% An that lies on the glomerocrystic trend and includes two small amphibole crystals (1 in Fig. 9b), suggesting rare mixing of trachydacitic magma with evolved crystal mush. Compositionally banded pumice JK068 has a bimodal distribution of plagioclase compositions (Fig. 9b). Unzoned plagioclase laths, zoned euhedral crystals, often in clots with olivine, clinopyroxene and brown interstitial glass (58–60 wt% SiO_2; Fig. 8) have compositions of 66–86 mol% An and occur in the dark zones where matrix plagioclase has 51–61 mol% An. These all straddle the glomerocrystic and knobbly lava Or-An trend (Fig. 9b). Plagioclase in the lighter zones is typically intensely zoned and plots on the main-pumice Or-An trend in the range $32 < An < 40$ mol%.

Olivine

All measured olivine crystals form a coherent trend of Ni decreasing from 1200 mg/kg to practically zero as Mg-number (based on total Fe) decreases from 84 to 64. In the type 1 and 2 knobbly lava samples (JK110, JK125b, C169) olivine crystals including both large phenocrysts and small microcrysts, have high Fo = 84–79 mol% contents without significant compositional zonation (Fig. 7c). Knobbly lava type 3 samples (JK075b, c) have lower and much more variable Fo = 81–54 mol%, with a clear bimodal distribution in JK114.

Olivine crystals in basaltic glomerocrystic clast JK003 range Fo = 79–72 mol%; olivine crystals in trachyandesitic glomerocrystic clast (JK049 Fo = 77–74 mol%, JK066a Fo = 76.5–75 mol%) appear to be inherited from mafic magma. However, one olivine core in JK066a and one crystal in an olivine cluster in JK049 have low Fo = 66–65 mol%, which indicates that that mafic magma had earlier entrained olivine crystals from a more evolved source.

The largely overlapping olivine compositions of type-3 knobbly lavas and glomerocrystic clasts suggest that Fo < 79 mol% olivine crystals in type-3 lava derive from the crystal mushes. The banded pumice JK068 contains two olivine populations of Fo = 82–77 mol% (Ni > 650 mg/kg) and Fo = 77–76 mol% (Ni < 510 mg/kg) likely derived from basaltic magma and from crystal mush, respectively.

Clinopyroxene and orthopyroxene

Clinopyroxene compositions in the knobbly lavas and glomerocrystic clasts cover a limited range of 70 < Mg# < 78 with a weak tendency of TiO_2 and Al_2O_3 to increase to lower Mg# (Fig. 10). Green dashed lines in Fig. 10 indicate a possible gap between low and high TiO_2 and Al_2O_3 glomerocrystic groups, respectively, but all glomerocrystic samples contain compositions from both groups. The almost identical TiO_2 and Al_2O_3 patterns in clinopyroxene reflect the good positive correlation between these elements (inset Fig. 10c). Orthopyroxene in glomerocrystic clasts generally has lower Mg# than that in the knobbly lavas but there is overlap due to the wide range found in JK049 (Fig. 10). Clinopyroxene and orthopyroxene crystals in the main pumice have limited Mg#-variations and typically low TiO_2 and Al_2O_3 contents distinguishing them clearly from the knobbly lava and glomerocrystic pyroxene crystals (Fig. 10). On

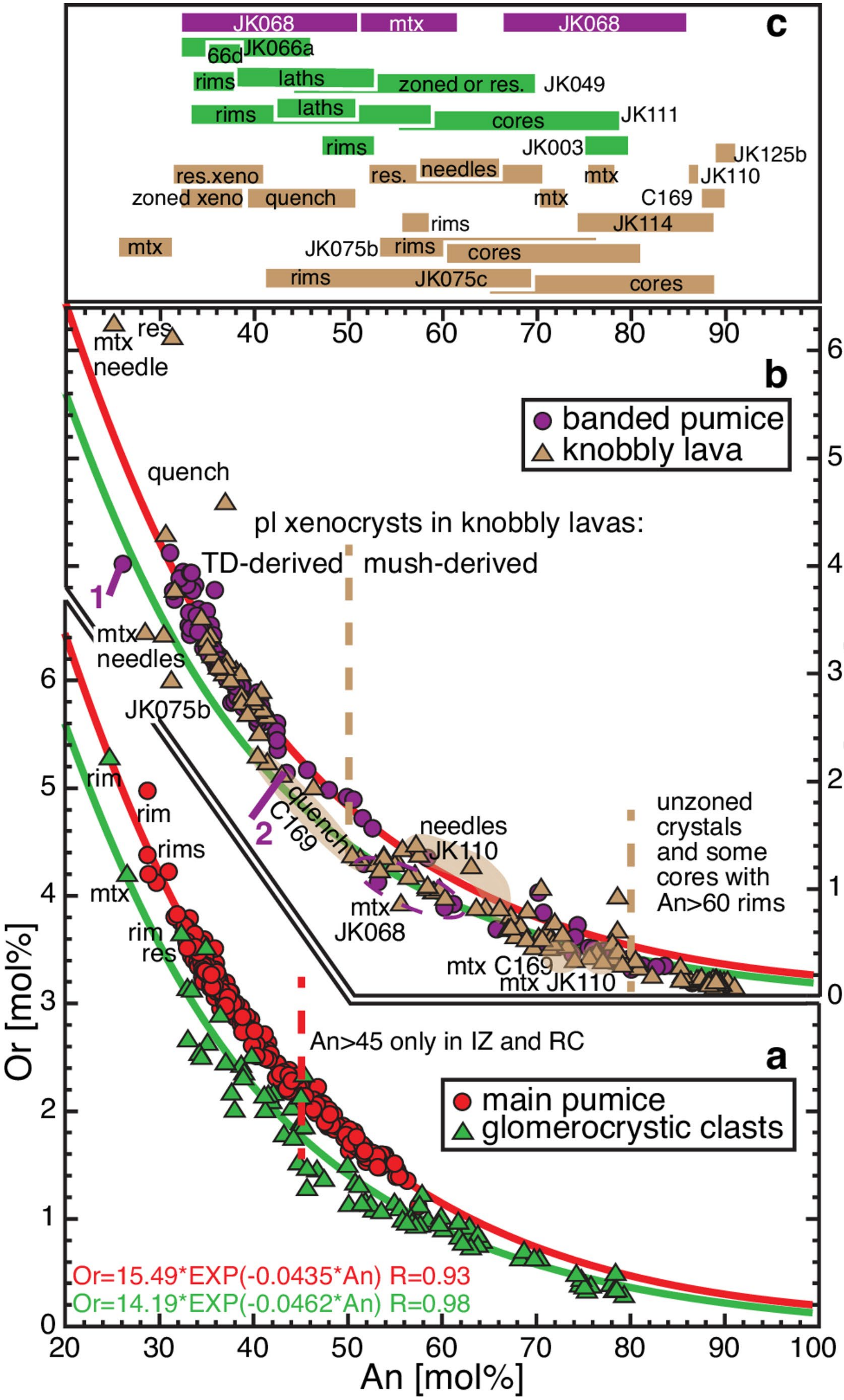
c
JK068
mtx
JK068
66d
JK066a
rims
laths
zoned or res.
JK049
rims
laths
cores
JK111
rims
JK003
JK125b
res.xeno
res.
needles
mtx
JK110
zoned xeno
quench
mtx
C169
rims
JK114
mtx
JK075b
rims
cores
rims
JK075c
cores
b
banded pumice
knobbly lava
mtx
res
needle
quench
pl xenocrysts in knobbly lavas:
TD-derived
mush-derived
1
mtx
needles
JK075b
2
C169
quench
needles
JK110
mtx
JK068
unzoned crystals and some cores with An>60 rims
mtx C169
mtx JK110
Or [mol%]
0
1
2
3
4
5
6
a
main pumice
glomerocrystic clasts
rim
rim
rims
mtx
rim
res
An>45 only in IZ and RC
Or=15.49*EXP(-0.0435*An) R=0.93
Or=14.19*EXP(-0.0462*An) R=0.98
Or [mol%]
0
1
2
3
4
5
6
An [mol%]
20
30
40
50
60
70
80
90
100

Fig. 9 Variations in plagioclase Or and An contents. (a, bottom) Plagioclase crystals from main pumice and glomerocrystic clasts define separate trends of Or vs. An; red and green lines are the regression functions (see lower left) through the respective data (R = coefficient of correlation). An >45 mol% compositions in main pumice only occur in resorbed cores (RC) and inner stratified zones (IZ). The highest-Or compositions are typically from rims and matrix crystals. (b, center) Or versus An variations for banded pumice and knobbly lava samples. The red and green regression lines from (a) are repeated for reference. True knobbly lava phenocrysts have An > 80 mol%. Other plagioclase crystals were entrained from trachydacite (An < 50 mol%) and from glomerocrystic material (An > 50 mol%). Apparently, no plagioclase from evolved glomerocrystic clasts (An <46 mol%) was entrained; the An <46 mol% compositions close to the glomerocrystic trend observed in knobbly lavas are from quenched matrix crystals. Matrix plagioclase in type-1 knobbly lava JK110 have An ~76 mol% compositions but in type-2 lava C169 An ~71 mol%. Low-An matrix needles in the glomerocrystic region of type-3 knobbly lava JK075b lie on the glomerocrystic trend. In banded pumice samples plagioclase of An <50 mol% lies on the main-pumice trend while crystals An > 50 mol% overlap with knobbly lava and glomerocrystic plagioclase compositions. Numbers 1 and 2 are referred to in the text. (c, top) Color-coded bars indicate the An-ranges of individual samples. mtx = matrix crystals, res = partially resorbed crystal, xeno = crystal interpreted as xenocryst

average, knobbly lava and glomerocrystic orthopyroxene has higher Al_2O_3 concentrations than orthopyroxene in the main pumice, but equal TiO_2 contents. Clinopyroxene and orthopyroxene crystals in banded pumices completely overlap with those of the main pumice, only a few clinopyroxene crystals (some associated with olivine and carrying a tachylitic mantle) have the high-Mg# compositions typical of knobbly lava or glomerocrystic clasts (Fig. 10).

Knobbly lava samples JK110 and C169 contain a few clino- and orthopyroxene xenocrysts derived from the trachydacitic magma; these are all attached to intensely zoned plagioclase. Glomerocrystic clast JK066a contains some orthopyroxene crystals that have a low-Al_2O_3 core composition (inside the main pumice field in Fig. 10b) overgrown by Mg#<55 rims, and glomerocrystic clast JK111 contains a low-Mg# clinopyroxene core (Fig. 10); these cores are all xenocrysts entrained from an evolved source during early stages of pyroxene crystallization.

It is noteworthy that clinopyroxene and orthopyroxene of any of the rock types never share the same Mg#; clinopyroxene always has higher Mg# and thus crystallized during an earlier stage of magmatic evolution than orthopyroxene. In knobbly lava sample JK075b Mg#'s of both pyroxenes do partly overlap at 71.5 to 74 (Fig. 10b) but these are clinopyroxene cores overgrown by high-Mg# rims and orthopyroxene cores overgrown by lower-Mg# rims, and thus were not in equilibrium.

Amphibole

Apart from a few hastingsitic matrix crystals, all amphibole crystals are magnesiohastingsites. Most amphibole crystals in the knobbly lava samples are limited to a narrow compositional range (Fig. 11). The only exceptions are skeletal amphibole needles in the matrix of the glomerocrystic region of type-3 sample JK075b (Fig. 6h) and amphibole needles from the quenched dark rims of large vesicles in type-2 sample C169 (Fig. 6e, f) which all have distinctly lower Mg# (Fig. 11). Type-1 knobbly lava (JK110, JK125b) only contains matrix amphibole.

Amphibole crystals in the evolved glomerocrystic clasts (JK066a, d) have low Mg# with limited variation in contrast to widely varying amphibole compositions in intermediate glomerocrystic clasts (JK049, JK111). Sample JK111 actually covers the entire observed Mg# range (Fig. 11) with the highest Mg# found in the largest crystals (Fig. 6b). Amphibole crystals in knobbly lava and glomerocrystic clasts are not or weakly zoned (Mg#-differences < 3 between core and rim) and there is no systematic compositional difference between amphibole included in plagioclase or amphibole attached to, and apparently replacing, clinopyroxene.

The rare, exceptional occurrences of amphibole in main pumice include small stubby euhedral crystals in JK057a, which compositionally overlap with amphibole in glomerocrystic clasts from which they were likely entrained (Fig. 11). The large rounded amphibole crystal in sample JK055 overlaps with lava and glomerocrystic amphibole compositions (Fig. 11) but has distinctly higher K_2O content (0.6 wt% compared to < 0.5 wt%) and is thus considered a xenocryst.

The banded pumice amphibole crystals in Fig. 11 have all been analyzed in one sample (JK112a). Yet they span practically the entire compositional range of amphibole in glomerocrystic clasts. The presence of Mg#>60 amphibole fits the presence also of Mg#>72 clinopyroxene (Fig. 10). Moreover, a lower-Al_2O_3 subgroup of small amphibole crystals (purple dashed line in Fig. 11a) are intergrown with a plagioclase that compositionally falls onto the glomerocrystic Or-An trend (Fig. 9b). The crystal load of banded pumice JK112a is thus a mixture of main-pumice (Pl, Cpx) and glomerocrystic-clast (Amp, Cpx, Pl) minerals.

Biotite

Evolved glomerocrystic clast JK066a is the only analyzed juvenile sample in which we found biotite. These isolated euhedral crystals have lower Mg#=50–52 than the amphibole crystals in that sample (Fig. 11) and likely form the last phenocrysts precipitated before eruption.

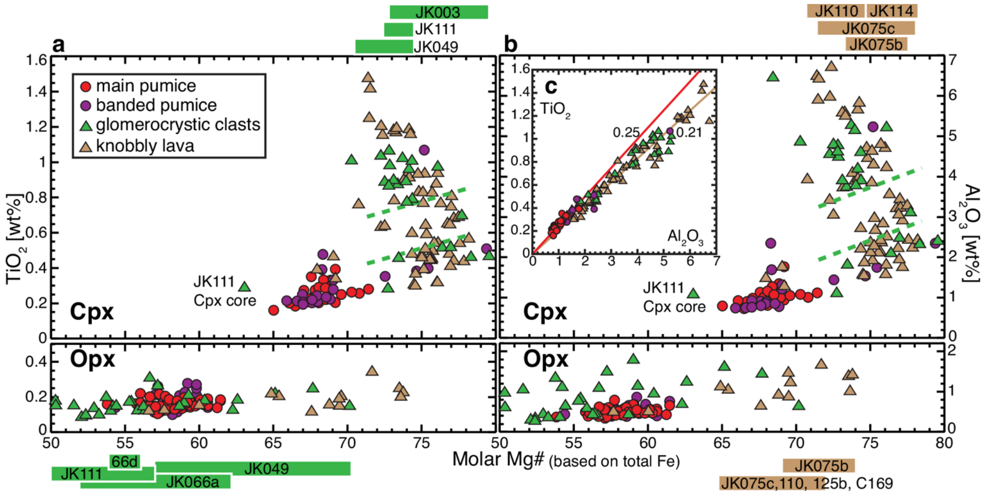

Fig. 10 (a) TiO_2 and (b) Al_2O_3 contents in clinopyroxene (upper panels) and orthopyroxene crystals (lower panels) versus molar Mg-number. Note much lower Mg# of orthopyroxene than of clinopyroxene crystals. Color-coded bars indicate the compositional ranges per sample for clinopyroxene (at top) and orthopyroxene (at bottom of graph). Green dashed lines indicate possible TiO_2 and Al_2O_3 gaps in the glomerocrystic-clasts clinopyroxene compositions. A low-Mg# clinopyroxene core (overgrown by high-Mg# clinopyroxene) in glomerocrystic clast JK111 is probably an early entrained xenocryst. Inset (c) illustrates good positive correlation between TiO_2 and Al_2O_3 in clinopyroxene crystals; line 0.21 gives the mean TiO_2/Al_2O_3 ratio for glomerocrystic and knobbly lava clinopyroxene while that for trachydacite clinopyroxene is slightly higher (0.25)

Fe–Ti oxides

Titanomagnetites in the four juvenile rock types have well-constrained compositions within a sample while all samples together form a good positive correlation between MgO and Al_2O_3 (Fig. S7). An exception is knobbly lava JK110 in which magnetite MgO contents vary independent of Al_2O_3. Rare Cr-rich magnetites occur in knobbly lava (< 0.23 wt% Cr_2O_3), banded pumice (0.47 wt%) and glomerocrystic clast JK111 (2.87 wt%). Minor ilmenite occurs in the main pumice and the main-pumice components in banded pumice. In these rocks both magnetite and ilmenite have very narrow compositional ranges (Fig. S7).

Equilibrium considerations and geothermobarometry

The petrographic and mineral-chemical evidence for mingling of the various magmatic components in most samples requires testing for equilibrium parageneses typically by experimentally established equilibrium partition coefficients. In most geothermobarometric formulations temperature (T), pressure (P), and melt H_2O-content (X_{H2O}) are mutually dependent and we performed the calculations in an iterative fashion in order to achieve an internally consistent data set. Bulk-rock and matrix glass compositions are obvious choices for melt composition for early and late-formed precipitates, respectively, but for crystals formed in-between we also calculate a "halfway melt" composition centered between the bulk-rock and glass compositions along the liquid line of descent. We did not use the few available melt-inclusion glasses because these occur in resorbed disequilibrium zones. We also do not consider banded pumices here since the disequilibrium risk is obvious. The geobarometric equations, their calibration errors (SEE) and our results are compiled in Table S8 in the supplement, which shows that the standard deviations around the average data for each sample, caused by the ranges of melt and mineral compositions, are mostly smaller than the SEE values. Table 1 provides a short overview of the temperature, pressure and water content ranges for each rock type but Table S8 should be considered for details.

Plagioclase-melt equilibrium

We use Eq. 24a, 25a, and 25b of Putirka (2008) as well as Eq. 14 of Waters and Lange (2015) to estimate T, P, and X_{H2O} values. In the main pumice, the cores (RC) and the outer margin (R) of the inner zone (IZ) of zoned plagioclase are typically resorbed (Fig. 5) and we only use plagioclase compositions < 45 mol% An from the outer (OZ) for thermobarometric calculations. Compositions 21–37 mol% An (Figs. 5 and 9) would be in equilibrium with matrix glass around 842 °C according to the partition coefficient $K_D(An\text{-}Ab)^{pl-liq} = 0.10 \pm 0.05$ (for T < 1050 °C; Putirka 2008). However, 64 of 72 pairs in the plagioclase range An = 29–45 mol% also fulfill the equilibrium criterion with a halfway melt composition around 863 °C (Table

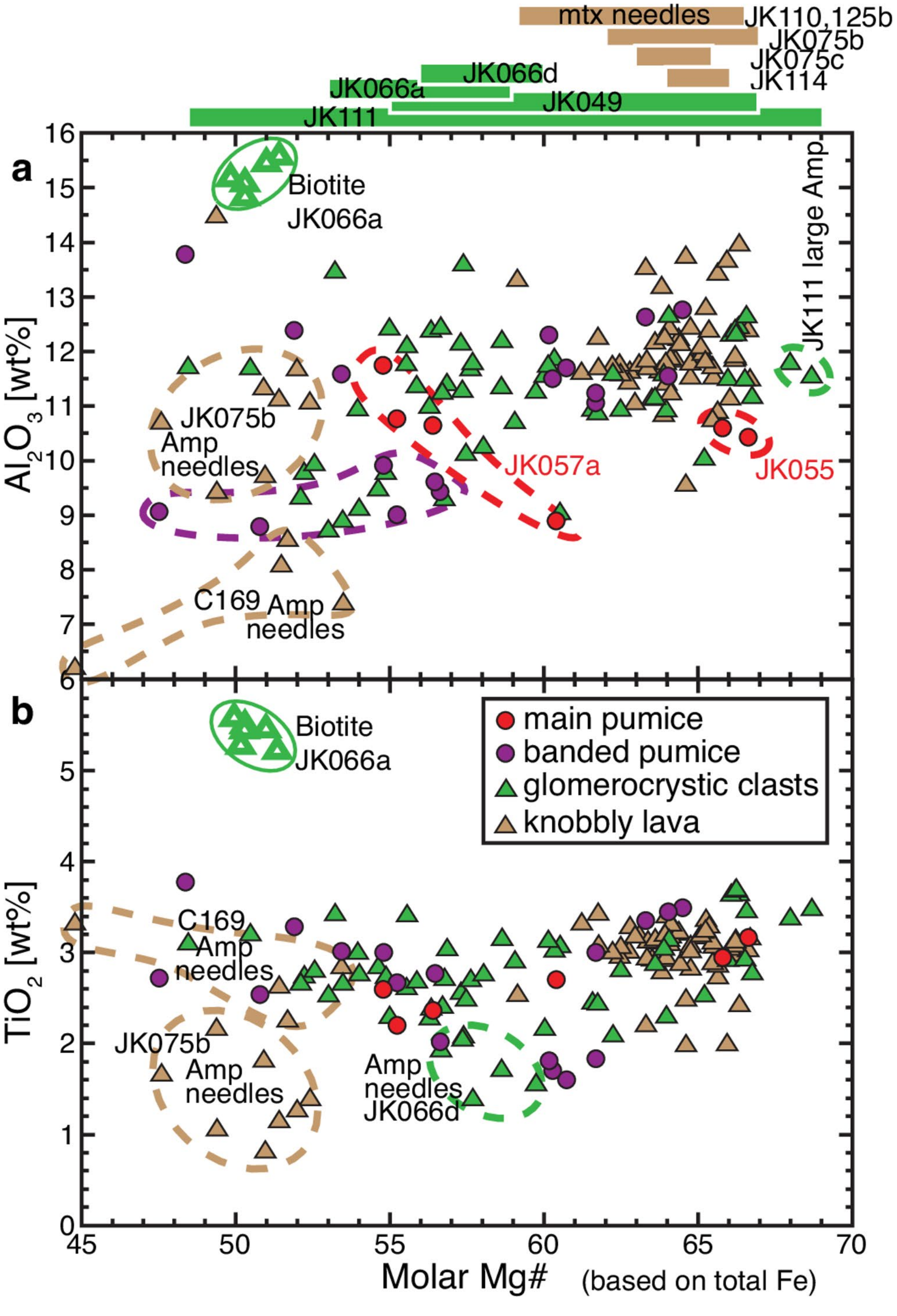

Fig. 11 (a) Al_2O_3 and (b) TiO_2 contents in amphibole crystals versus Mg-number. Amphibole only forms needle-shaped matrix crystals in type-1 knobbly lavas JK110, JK125b. Amphibole needles in type-2 knobbly lava C169 are exclusively from the quenched vesicle rims (Fig. 6e, f). Dashed lines enclose data discussed in the text. Color-coded bars at top indicate the compositional ranges per sample. Open green triangles are the compositions of biotite in evolved glomerocrystic clast JK066a

S8). Estimated water contents of the melt lie around 4 wt% (Table 1, S8).

The mafic glomerocrystic clast JK003 has less evolved glass (Fig. 8) that could be in equilibrium with plagioclase 47–53 mol% An of the rim compositions (Fig. 9c) giving T = 948–969 °C and 2.7–3.9 wt% H_2O while a bulk-rock melt composition with plagioclase An = 75–79 mol% yields 1123 °C and 2.4 wt% H_2O (Table 1, S8). We found no equilibrium with matrix glass in intermediate glomerocrystic clast JK111 but halfway and bulk-rock melts yield 970 °C (4.2 wt% H_2O) and 1043 °C (3.4 wt% H_2O), respectively. In glomerocrystic clast JK049 bulk-rock, halfway and glass melt compositions produce a consistent decrease of temperature from 1069 °C to 971 °C to 867 °C (and H_2O increase from 2.8 to ~4 wt%; Table S8). For the evolved glomerocrystic clasts JK066a and JK066d halfway-melt

Table 1 Selection of temperature, pressure and water content data calculated from mineral-melt equilibria. See supplement table S8 for full data set

Sample type	Crystallization Temperatures (°C)									Pressure range (MPa)	Pressure W&B24	Melt H2O content (wt.%)	
	ol	cpx	opx	opx mtx	amp	amp mtx	mag-ilm	pl	pl mtx			Max	Min
Typical calibration error SEE	± 29 °C	± 42 °C	± 39 °C	± 39 °C	± 56 °C	± 56 °C	± 40 °C	± 36 °C	± 36 °C	> ± 160 MPa	> ± 110 MPa	± 0.35–1.1 wt%	
Main pumice trachydacite	no ol	911	902	857	no amp	no amp	872 bt ± 50 °C	863	842	275–64	wr 161 ± 12 gl 216 ± 44	4.7	3.9
Glomerocrystic evolved	no eq	no cpx	903	849–826	975–851	no eq	859	912	841–801	342–174	wr 243 gl 135–159	5.7	4.0
Glomerocrystic intermediate	1089–1023	1030–1006	1033–970	879–839	1024–946	925–818	no ilm	1069	867	321–79	(wr 315–371) gl 121–134	4.2	2.5
Glomerocrystic mafic	1172–1031	1097	no opx	no opx	no amp	no amp	no ilm	1123	948	345–260	(wr 273) (gl 387)	3.9	2.3
Knobbly lava basalt type 1	1112	1062	no eq	no eq	no pheno	no eq	no ilm	1052–1018	no eq	409–115	wr 299 (gl 177)	4.5	3.4
Knobbly lava basalt type 2	no eq	n.a	no eq	no eq	no pheno	837–814	no ilm	1051–1018	no eq	205–132	wr 149 gl 102	3.6	2.6
Knobbly lava mixed type 3	1119–1026	1081–1028	no eq	no eq	1006–931	926–787	no ilm	1145–1006	878–831	424–34	wr 174–308 gl 185	5.3	3.7

W&B24 Liquid-only barometry of Weber and Blundy (2024). Numbers in brackets = only high-variance large-error solutions found

no eq. = no equilibrium, n.a. = not analyzed, no pheno. = no phenocrysts of that mineral phase, wr = bulk-rock, gl = matrix glass results indicate 912 °C and 886 °C (5 and 5.7 wt% H_2O) while only three plagioclase-glass equilibrium pairs give temperatures of 801–841 °C and melt water contents of 4.5–4.8 wt% (Table 1, S8).

We have identified An =86–89 mol% plagioclase (Fig. 9b, c) as the early precipitated equilibrium phenocryst composition of types-1 and 2 knobbly lava samples and combined with bulk-rock melt composition this yields ~ 1052 °C and 4.5 wt% H_2O (Table 1, S8). For sample C169 a halfway melt with lower An =64–73 mol% plagioclase yields 1018 °C and 3.5 wt% H_2O (Table 1, S8). Type-3 knobbly lavas produce apparently plausible and consistent results but these must be considered with care due to the basalt-glomerocrystic mixed nature of these samples. However, plagioclase matrix needles in JK075b fit the matrix glass composition resulting in ~ 831 °C and 4.8–5.3 wt% H_2O. Similarly, matrix equilibrium indicates 878 °C and 3.7 wt% H_2O for JK075c (Table 1, S8).

Olivine-melt equilibrium

We used the Roeder and Emslie (1970) $K_D(\text{Fe-Mg})^{ol-liq}=0.3 \pm 0.05$ to estimate Fo contents of olivine in equilibrium with melt compositions, and Putirka's (2008) Eqs. 15 and 22 to estimate temperature. Only the three most Mg-rich (Fo ≥ 77 mol%) olivine crystals of mafic glomerocrystic clast JK003 satisfy equilibrium with the bulk-rock composition (1172 °C) but most crystals reach K_D values 0.2–0.23, not much below the limit $K_D \geq 0.25$, with a halfway melt composition (1031 °C; Table S8). The four measured olivine crystals in JK049 yield temperatures of 1089 °C to 1023 °C (Table 1, S8).

In knobbly lava sample JK110 olivine crystals (79–83 mol% Fo) in equilibrium with bulk-rock melt yield 1112 ± 2 °C (Table S8). In crystal-rich sample C169, however, olivine crystals Fo > 80 mol% formed from melt more mafic than the bulk-rock composition. Knobbly lava JK114 olivine crystals of Fo ≥ 72 mol% would be in equilibrium with bulk-rock composition (1119 °C) and olivine crystals of Fo < 72 mol% would be in equilibrium with a halfway melt (1026 °C). In sample JK075b olivine crystals are either too Mg-poor for the bulk-rock composition or too Mg-rich for the matrix composition but would fit a halfway melt at T = 1048 °C. In JK075c most olivine crystals (Fo = 71–77.5 mol%) yield around 1091 °C with a bulk-rock melt.

Pyroxene-melt equilibria

Equations (28a, b, 29a) and (33, 34, 32a, b, c) of Putirka (2008) allow to determine crystallization and saturation temperatures and crystallization pressure of orthopyroxene and clinopyroxene, respectively. The Mg-Fe partition coefficient between clinopyroxene and melt is approximately $K_D(\text{Mg-Fe})^{cpx-liq}=0.28 \pm 0.08$ (Putirka 2008) but is temperature-dependent (Eq. 35 of Putirka 2008) and we determined it's value *a posteriori* from the calculated temperature to verify equilibrium. The calculated crystallization temperature using melt H_2O content determined by plagioclase hygrometry should be equal or lower than the saturation temperature. The crystallization pressure values from the four barometer calibrations vary widely (Table S8) and can only be used to constrain crystallization of the Alpehué magmatic components in the upper crust.

No clinopyroxene compositions were in equilibrium with any matrix glass and all calculations assume bulk-rock melt composition. For the main pumice, in which clinopyroxene is obviously an early-formed phase that later became unstable as orthopyroxene precipitated, crystallization temperature is well constrained to around 911 ± 14 °C. For glomerocrystic clasts and knobbly lavas the crystallization temperatures differ by sample but all lie between 1000 °C and 1100 °C (Table 1, S8).

The partition coefficient $K_D(\text{Mg-Fe})^{opx-liq}=0.29 \pm 0.06$ decreases to higher silica contents of the melt (Putirka 2008) giving values of 0.24 for bulk-rock and 0.22 for glass compositions of the main pumice. As a result of the relatively small compositional differences between bulk-rock and glass compositions, particularly the Mg/Fe ratio, compared to the uncertainty in the K_D value, orthopyroxene compositions (Mg# 59.3 ± 1.5) better fitting bulk-rock do not differ much from those (Mg# 57.1 ± 1.2) better fitting glass composition. Most orthopyroxene crystals in the main pumice probably crystallized while the melt evolved towards the glass composition across the temperature interval from 902 °C to 857 °C (Table 1, S8), slightly lower than the respective saturation temperatures.

In the glomerocrystic clast samples orthopyroxene Mg-numbers mostly are too low for bulk-rock and too high for matrix glass melt compositions. Orthopyroxene crystals in glomerocrystic clast JK111 are tiny and mostly euhedral and are expected to be in equilibrium with matrix glass but for the results in Table S8 we needed to accept deviations up to ± 0.08 from the equilibrium K_D. For glomerocrystic clast JK049 rare orthopyroxene crystals fit bulk-rock or glass-like melt compositions while most of the analyzed small orthopyroxene crystals would fit equilibrium with a halfway melt. Thus, orthopyroxene in this glomerocrystic clast may have crystallized over a temperature interval from 1033 °C to 970 °C to 879 °C (Table 1, S8), agreeing with the relatively wide compositional range (Fig. 10). For evolved glomerocrystic clasts JK066a and JK066d orthopyroxene compositions deviate by ± 0.09 from equilibrium K_D for matrix-glass and the calculated temperatures of 826–903 °C and 849 °C, respectively, remain uncertain.

Amphibole-melt equilibrium

Next to petrographic evidence for equilibrium such as amphibole replacing clinopyroxene, chemical equilibrium criteria include the amphibole-melt Mg-Fe partition coefficient $K_D(\text{Fe-Mg})^{\text{amph-liq}}=0.28\pm0.11$ (with 10th to 90th percentile ranging 0.13–0.41; Putirka 2016) as well as a difference <7 wt% in melt silica content as observed and calculated from amphibole composition (Eq. 10 of Putirka 2016; with SEE of ±3.6 wt% SiO_2). Amphibole crystallization temperatures can be determined with Putirka's (2016) Eqs. 4a, 4b and 5 independent of pressure and with little sensitivity to melt H_2O (<2 °C per 1 wt% H_2O). Significant temperature difference between Eqs. 4a and 4b (Table S8) are possibly due to different closure temperatures for Na and Ti exchange (Putirka 2016). Crystallization pressure can be determined from Eqs. 7a and 7b (Putirka 2016) independent of temperature but sensitive to melt water content as ~40 MPa per 1 wt% H_2O.

We have interpreted the very rare amphibole crystals in main pumice as xenocrysts (Fig. 11) and using the amphibole-only thermometer (Eq. 5) suggests they derive form a source in which they crystallized at 907–922 °C. In glomerocrystic clast JK111, amphibole with Mg#>60 would be in equilibrium with a bulk-rock melt, other compositions with a halfway melt, but none with matrix glass composition. These amphibole crystals precipitated over a limited temperature range (1012–991 °C from Eq. 4a, 950–905 °C from Eq. 4b; Table S8) considering the wide range of JK111 amphibole compositions (Fig. 11). In glomerocrystic clast JK049, only the amphibole with the lowest Mg#=55 (Fig. 11) shows equilibrium with matrix glass, only amphibole with Mg#>62 would be in equilibrium with bulk-rock composition, and the majority would be in equilibrium with halfway melt, all together reflecting a crystallization interval from ~1033 °C to ~880 °C. Against expectation, the small amphibole crystals in the most evolved, fine-grained and glass-rich glomerocrystic clasts JK066a, d yield no chemical equilibrium with matrix glass but with halfway melt composition (967–975 °C from Eq. 4a, 851–877 °C from Eq. 4b).

The Mg-numbers (Mg#>64, Fig. 11) of amphibole needles in the matrix of knobbly lava JK110 are too high for equilibrium with matrix glass. Knobbly lava C169 only has amphibole matrix needles ($45<\text{Mg\#}<53$; Fig. 11) in the quenched rims of vesicles (Fig. 6e, f), which appear to satisfy chemical equilibrium with the matrix glass in those rims (814–840 °C; Table S8) but quench growth was probably not in equilibrium. This also applies to quench growth of the low-Mg# amphibole needles in JK075b (Figs. 6h and 11) in apparent equilibrium with the glomerocrystic-region glass, yielding diverging temperatures (926 °C from Eq. 4a, 787 °C from Eq. 4b). All amphibole phenocrysts and amphibole replacing clinopyroxene in JK075b and JK075c yield equilibrium with a halfway melt composition at around 1004–1012 °C (Eq. 4a) or 931–939 °C (Eq. 4b) but must be considered with care due to the mixed nature of the rocks. Amphibole phenocrysts in knobbly lava JK114 have a narrow range of compositions (Fig. 11) and resulting temperatures (Eq. 4a: 1010–1012 °C, Eq. 4b: 939–985 °C) are very similar for both bulk-rock and halfway melt compositions (Table S8). Temperatures obtained with the amphibole-melt thermometer of Molina et al. (2015), independent of pressure and melt water content, agree reasonably well with those from Eq. 4b in glomerocrystic clasts, better fit Eq. 4a results in knobbly lava samples, and in C169 they disagree with both equations.

Next to amphibole-melt equilibria, amphibole compositions alone can be used to estimate amphibole crystallization pressures. Mutch et al. (2016) calibrated an Al-in-amphibole barometer and barometric Eqs. 1b and 1c of Ridolfi and Renzulli (2012) are based on the entire amphibole composition. These barometers give similarly diverging results as from pyroxene barometry (Table S8).

Biotite-melt equilibrium

Biotite precipitated as a late phenocryst phase in evolved glomerocrystic clast JK066a and was probably in equilibrium with melt of matrix glass composition. The Ti-exchange thermometer (±50 °C uncertainty; Righter and Carmichael 1996) yields temperatures of 859 ± 13 °C from measured biotites and average Ti content of the glass (Table 1, S8).

Magnetite–Ilmenite equilibrium

Only in the main pumice is the omnipresent titanomagnetite accompanied by ilmenite and both have very narrowly confined compositions. Ilmenite and magnetite pairs match equilibrium Mg/Mn partitioning (Bacon and Hirschmann 1988). We used the mineral recalculation scheme of Stormer (1983), the thermobarometer of Anderson and Lindsley (1985), and the spreadsheet of Lepage (2003) to calculate crystallization temperatures of 872 ± 13 °C with oxygen fugacity ($\log fO_2=-12.27\pm0.24$) at the level of the NNO buffer (Table 1, S8).

Liquid-only thermobarometry

Weber and Blundy (2024) recently introduced a machine learning-based model which derives magmatic temperature and pressure from comparing a melt composition saturated with given mineral phases with a huge experimental data base. This random forest method involves a large number of decision trees in analyzing the data and removing outcomes with high variance can improve the accuracy of prediction. Under optimal conditions, uncertainties can be as low as ±21° for temperature and ±110 MPa for pressure. We applied the method (a) to the bulk-rock compositions of the Alpehué component magmas assumed to have been saturated with their early-formed phenocryst phases, and (b) to the matrix glass compositions assumed to have been saturated with the late-formed phenocrysts and matrix crystals. Results in supplement Table S9 overlap with results in Table S8 obtained by traditional calibration methods. Results with low variances (red and green in Table S9) yield 161 ± 12 MPa and 216 ± 44 MPa pressure for trachydacite bulk-rock and glass, respectively, 243 MPa (bulk rock) and 125–159 MPa (glass) for evolved glomerocrystic mush, 121–134 MPa (glass) for intermediate mush, and 150–300 MPa (bulk-rock) and < 223 MPa (glass) for knobbly lava basalt (Table 1). Pressures larger than 400 MPa only result from models with large variances.

Discussion

Magma storage conditions

Most of the thermohygrometric calculations yield crystallization temperatures with relatively small errors and reasonably well constrained melt water contents. Figure 12 illustrates temperature and H_2O data obtained from plagioclase-melt equilibria. These data show an average decrease in temperature with increasing melt H_2O content (−93°/wt% H_2O) similar to, but steeper than, the experimentally determined drop in plagioclase liquidus (−42°/wt% H_2O; Almeev et al. 2012). On average, crystallization during cooling (from 1150 °C to 950 °C) enriched water in the residual melt from ~2 to ~4 wt%, a factor ~2 enrichment (i.e., ~50% crystallization) comparable to Zr enrichment over that interval (Fig. 3b). The associated average crystallization rate of 0.25%/−1 °C lies in the range observed in petrologic experiments (0.24%/−1 °C for trachybasalt, Barclay and Carmichael 2004; 0.3%/−1 °C for dacite, Costa et al. 2004). The maximum temperatures found for precipitation of the phenocryst phases in the glomerocrystic clasts and knobbly lavas agree reasonably with the respective

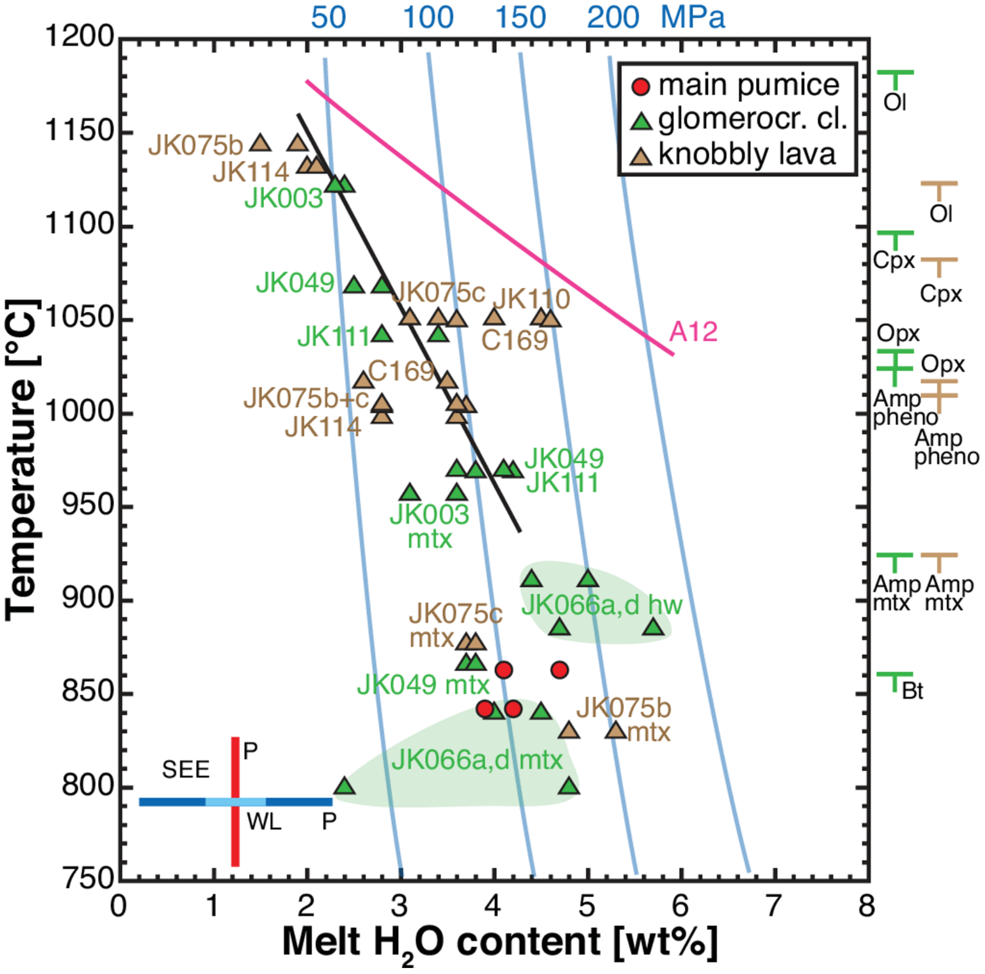

Fig. 12 Temperature-melt H_2O diagram summarizing plagioclase-liquid thermohygrometric results. These are not individual calculations but the mean values reported in Table S8 using whole-rock or matrix-glass (mtx) melt compositions. Green fields include halfway-melt (hw) and matrix-glass results for evolved glomerocrystic clasts JK066a, d (see Table S8). Maximum calculated temperatures for other mineral phases are indicated outside the right margin for comparison. Thin blue near-vertical lines show water saturation at the pressures indicated at top after Liu et al. (2005). Bold black line is a linear regression through the data down to 950 °C that implies a steeper temperature decrease to higher H_2O than the experimentally determined change in plagioclase liquidus temperature (A12, magenta line) of Almeev et al. (2012). Error cross at lower left indicates the calibration errors (SEE) for temperature (±36°) and water content (±1.1 wt% and ±0.35 wt%) after P = Putirka (2008) and WL = Waters and Lange (2015), respectively

experimentally determined phase boundaries for mafic compositions (cf. Melekhova et al. 2017; Feig et al. 2006; Berndt et al. 2005). For silicic compositions the calculated water contents satisfy experimentally determined stability of orthopyroxene (cf. Scaillet and Evans 1999; Costa et al. 2004). All these observations support the plausibility of the calculated thermohygrometric data.

The experimental amphibole phase boundaries vary greatly particularly with respect to the minimum water contents required to stabilize amphibole below ~900 °C (cf. Scaillet and Evans 1999; Costa et al. 2004; Sato et al. 1999) but melt water contents of the amphibole-bearing evolved glomerocrystic clasts (JK066a, d) and the amphibole-free main trachydacitic magma are similarly high and cannot explain the difference in amphibole phenocryst precipitation. Bulk-rock compositions, particularly Na_2O contents, are also similar (Fig. 2, S4) leaving storage pressure as the controlling factor.

The average of all barometric results in Table S8 is 265 ± 166 MPa with a total range of 0–700 MPa, which places residence of the Alpehué magmas in the upper half of the crust (MOHO depth is ~40 km or ~1000 MPa; Sielfeld et al. 2019). Liquid-only thermobarometry after Weber and Blundy (2024) places the Alpehué magmas at < 300 MPa pressure (Table 1, S9). However, the mineral barometric methods produce conflicting data and cannot resolve pressure differences between the magmatic components due to their large uncertainties. Therefore, we need other criteria to constrain the vertical succession of storage of the component magmas.

(1) The storage depth of the main trachydacite magma is constrained by two conditions: the absence of amphibole and the saturation pressure of ~100 MPa of its ~4 wt% dissolved H_2O (Fig. 13a). At the temperature range $872-857 \pm 40$ °C for Fe-Ti-oxide and orthopyroxene phenocrysts, i.e. those formed last before quenching during eruption, the minimum pressure needed to stabilize amphibole determined in petrological experiments on (trachy-)dacitic compositions ranges from 70 to 210 MPa (Fig. 13a). The (unknown) amphibole stability limit for the Alpehué trachydacite must lie at higher than ~100 MPa pressure (red dashed line, Fig. 13a).

(2) At the temperatures of the last-formed phenocrysts orthopyroxene, amphibole and biotite ($859-827 \pm 48$ °C), the ~5 wt% dissolved H_2O of the evolved glomerocrystic clasts (JK068a, d) indicate a saturation pressure of ~150 MPa, which must be larger than the minimum pressure of amphibole stability for that composition (Fig. 13a) due to the abundant amphibole phenocrysts.

(3) We argue below that the glomerocrystic samples derive from one crystal-mush reservoir that was compositionally zoned from lower mafic to upper evolved bulk composition. No large-volume eruptions which could have formed the ~6 km^3 caldera are known from Sollipulli (Gilbert et al. 1996; Lachowycz et al. 2015) and the ~8 km^3 Alpehué tephra appears to be the biggest known event. Therefore, the crystal-mush reservoir probably had a few km^3 volume at most and just a few kilometers vertical extension suggesting a top to bottom pressure difference of roughly ~50 MPa. We therefore place the intermediate and mafic glomerocrystic clasts in the 150–200 MPa pressure interval (Fig. 13a).

(4) The rising mafic magma of the knobbly lava clasts has entrained glomerocrystic material from the crystal mush and thus ascended from a deeper storage level. The pressure values with the smallest error derived from bulk liquid compositions (Weber and Blundy 2024) suggest mafic magma storage at 150–300 MPa pressure (Table 1, supplement Table S9) which fits the region below the crystal-mush reservoir (Fig. 13a).

In summary, we propose a vertical succession from deeper mafic magma through mafic to evolved crystal mush to upper main pumice reservoirs (Fig. 13b). The vertical separation between amphibole-free trachydacite and deeper-lying amphibole-bearing crystal mush is also supported by higher orthopyroxene Al_2O_3 contents (0.58 ± 0.25 wt%) in the glomerocrystic clasts compared to 0.46 ± 0.09 wt% in the main pumice (Fig. 10b). The estimated storage pressures of ~100 MPa for trachydacite magma and ~150 MPa for evolved glomerophyric mush are, of course, subject to the uncertainty in determining the respective dissolved water contents.

The overall low-pressure crystallization of the mafic to intermediate rocks is supported by (1) high plagioclase temperatures, (2) large overlap between plagioclase and clinopyroxene crystallization observed petrographically and thermometrically, suggesting proximity to the low-pressure (~100–150 MPa) crossover of the two phase boundaries (e.g., Moore and Carmichael 1998; Hammer et al. 2002; Feig et al. 2006), and (3) relatively high Cpx-out temperatures (cf. Melekhova et al. 2017) marked by replacement by amphibole. However, the wide ranges and bimodality of clinopyroxene Al_2O_3 contents in glomerocrystic clasts and knobbly lavas (Fig. 10b) are evidence for polybaric evolution of these magmas probably before precipitation of amphibole phenocrysts with relatively limited Al_2O_3 variation (Fig. 11). The estimated storage pressures for less evolved glomerocrystic clasts and knobbly lavas imply that these magmas remained water-undersaturated in their reservoirs (Fig. 13a).

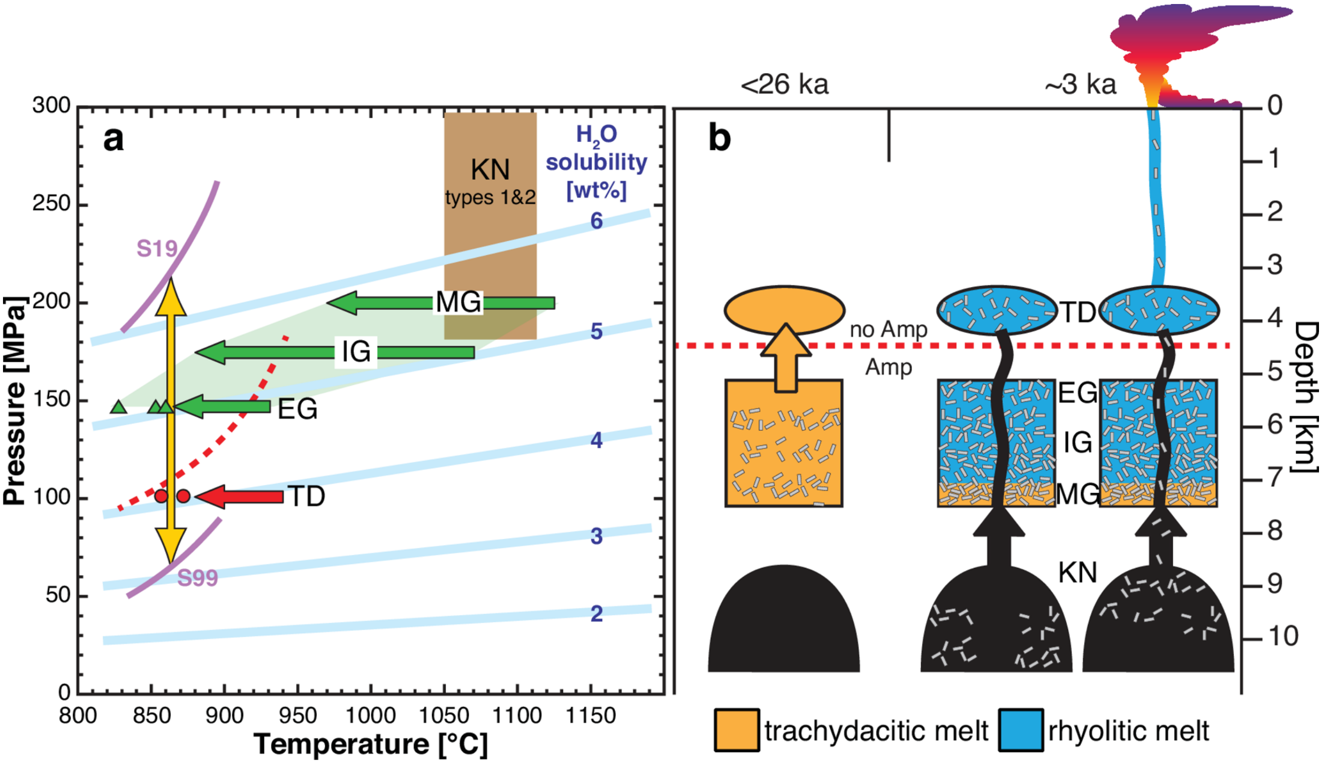

Fig. 13 (a) Schematic illustration of the interpreted arrangement of the Alpehué component magmas in pressure-temperature space. Blue bars are water solubilities calculated after Moore et al. (1998). Amphibole stability boundaries experimentally determined for (trachy)dacitic compositions distribute over a wide pressure range (orange double arrow) at around 850–870 °C, from low pressure in Sato et al. (1999) (S99) to high pressure in Solaro et al. (2019) (S19); examples of intermediate amphibole boundaries can be found in First et al. (2021), Holtz et al. (2005) and Voigt et al. (2022). Red dashed curve is a theoretical amphibole boundary curve separating trachydacite TD and evolved glomerocrystic mush (EG). Intermediate (IG) and mafic (MG) mush zones lie deeper in the zoned mush reservoir (green field) which probably did not extend over a pressure interval much greater than ~50 MPa. Knobbly lava (KN) type 1 and 2 basaltic magmas resided below the crystal-mush reservoir. Red arrow indicates (Pl, Cpx) crystallization temperature range down to Mag-Ilm and Opx temperatures (red dots). Green arrows indicate crystallization temperatures of glomerocrystic clasts with late Opx, Amp, Bt crystallization (green triangles) shown for EG. Width of brown field shows range of Ol, Pl, Cpx crystallization temperatures of knobbly lava. (b) Schematic illustration of magma reservoir arrangements under Sollipulli. An upper intermediate reservoir, underlain by a basaltic reservoir and both probably related to pre-Alpehué eruptions > 26 kyrs ago, had largely crystallized to trachydacitic melt composition. Escaping melt formed a shallower, separate reservoir in which it further crystallized mainly complex-zoned plagioclase (Fig. 5). At the time (3 ka) of the Alpehué eruption, the trachydacite and crystal-mush reservoirs had both largely differentiated to rhyolitic melt (Fig. 8). Crystal-poor type-1 basalt magma penetrated the mush and trachydacite reservoirs, followed by crystal-rich type-2 basalt that ultimately triggered the eruption

Evolution of the main trachydacitic magma

With no obvious stratigraphic variations in composition, the main pumice represents a crystal-rich (14–29 vol%) erupted trachydacitic magma body with little zonation. However, the co-magmatic obsidian fragments (O1 in Figs. 2 and 4) may derive from a crystal-poor rhyolitic melt layer at the top of the reservoir. The geochemical data (Figs. 2, 3 and 4 and S4, S5) are compatible with the trachydacite having differentiated from the range of magmatic compositions indicated by the knobbly lava and glomerocrystic clasts. As argued above, the original trachydacitic magma must have separated from its parental reservoir to be emplaced at shallower level where amphibole was no longer stable. Probably it formed as crystal-poor residual melt that escaped from a crystal mush with trachydacitic melt composition (Fig. 13b) by compositional convection, hindered settling, compaction or tectonic forces (Tait et al. 1984; Holtzman et al. 2003; Holness et al. 2017; Cashman et al. 2017). This trachydacitic melt had a Zr content of around 250 mg/kg (Fig. 3b) which would be compatible with residual melt of an intermediate magma mush at about 45–50% crystallinity, the most efficient range for melt escape (Bachmann and Bergantz 2004, 2008). After separation, the trachydacite magma crystallized and evolved further as shown by its large complex-zoned plagioclase crystals (Fig. 5), its bulk geochemical variations (Figs. 2, 3 and 4 and S4, S5) and its rhyolitic matrix glass (Fig. 8). The Alpehué trachydacite differentiated in slightly different fashion than older Sollipulli trachydacites (Figs. 3 and 4b, S4c), which erupted up to ~20,000 years before the Alpehué eruption (Lachowycz et al. 2015). This time interval is sufficiently long for the

Alpehué trachydacite reservoir to develop independently (cf. cooling and crystallization time scales in Hawkesworth et al. 2000; Cooper 2019).

The more potassic nature of the trachydacite magma produced more Or-rich plagioclase compared to the less evolved magmas (Figs. 2b and 9); other factors favoring Or-rich plagioclase such as temperature or pressure differences are insignificant in the upper-crustal situation considered here (Sato 1984; Sun et al. 2017; Bedard 2006). Partition coefficients for such plagioclase compositions (D(Ba) > D(K) > D(Rb); Bedard 2023) made Rb less, but Ba more compatible than K and also relative to Zr which explains the deviation of the trachydacite compositions from the trend through mafic to intermediate compositions in the respective diagrams (Fig. 3).

The internal stratigraphy of growth and resorption zones (Fig. 5) is basically the same in all analyzed large zoned plagioclase crystals which indicates that the ambient changes probably affected almost the entire trachydacite reservoir rather than just local areas (cf. Pietranik et al. 2006). The resorbed cores (RC) with patchy extinction patterns commonly have An > 45 mol% (Figs. 5c and d and 9) but can also include patches of lower An-contents (Fig. 5a, b). The origin of the plagioclase cores is uncertain. Resorption of antecrysts by decompression requires significant pressure reduction (Nelson and Montana 1992; Bennett et al. 2019) while we do not see evidence for any deep-crustal involvement. Probably the cores have been entrained as xenocrysts that became partially resorbed and experienced recrystallization to equilibrium An contents in the resorbed patches (e.g. Vance 1965; Humphreys et al. 2006). Alternatively, the observation that the labradoritic cores (RC) overlap in composition with the inner zoned mantle (IZ) (Fig. 5) suggests that the cores may represent initial skeletal plagioclase growth followed by subsequent filling of the gaps (Kuo and Kirkpatrick 1982; Tsuchiyama 1985; Bennett et al. 2019) and equilibrium overgrowth (IZ). Skeletal growth can already occur at low degrees of supercooling (Kuo and Kirkpatrick 1982) which may have occurred when the initial (crystal-poor) trachydacite magma ascended from its hotter source in the crystal mush body to a cooler higher level.

Continued equilibrium growth was interrupted by formation of the resorbed zone (R) across which plagioclase An-contents drop by > 5 mol% (Fig. 5), immediately followed by an increase in An-content in the outer mantle OZ. The undular and locally discordant contact of zone R to zone IZ is evidence for true dissolution and resorption but the melt inclusions in R, which compositionally overlap with matrix glasses (Fig. 8), provide no evidence for a significant shift to less evolved melt composition. We therefore interpret that resorption was caused by sudden heating which shifted equilibrium to higher-An plagioclase. According to the plagioclase solidus slope at An ~ 40 mol% (at P_{H2O}=200 MPa; Johannes 1989) ≤ 10° heating could cause a ≤ 10 mol% increase in equilibrium An content. While the event that caused resorption in zone R was the strongest, it was not the only one. Oscillations in the overall outward decreasing An content and unconformities in the fine stratification of the outer zoned mantle (OZ) (see microphotographs in Fig. 5) suggest repeated minor heating events during crystallization (cf. Ginibre et al. 2002). While resorption zone R may document a strong episode of underplating hot magma the enhanced convection of the resident trachydacite magma may be responsible for recurrent heating of the growing plagioclase crystals. Another speculative heat source could be hot fluids that escaped from the deeper crystallizing mush reservoir (e.g., Parmigiani et al. 2017; Degruyter et al. 2019) but these would probably only have local effects.

Banded pumice

Samples in which textural banding is not associated with compositional differences probably formed by shearing during ascent in the conduit. In these shear zones vesicles are smaller and crystal fragments are abundant compared to the less or not sheared regions (cf. Polacci et al. 2001). Other banded pumices, however, were formed mainly by mixing between the basaltic to basaltic-andesitic and trachydacitic magmas but also involving inflated glomerocrystic material. An example is sample JK068 (Fig. 1c) in which quenched low-silica melt (Fig. 8), high-An plagioclase (Fig. 9), and high-Mg# (77–82) olivine, pyroxenes and amphibole (Figs. 10 and 11) coexist with the main-pumice mineral assemblage. The absence of disequilibrium reactions, the preservation of quenched sideromelane, and the presence of abundant angular crystal fragments support shearing and mingling in the conduit during eruption. Moreover, the olivine and sideromelane-bearing zones demonstrate that some liquid mafic magma reached the vent exit next to the microlite-rich knobbly lava clasts that were quenched at depth.

Origin of the glomerocrystic clasts

All glomerocrystic clasts apparently crystallized at shallow depths but above the minimum pressure for amphibole stability. Their common liquid line of descent (Figs. 2, 3 and 4) supports their origin from a coherent crystal mush body that was zoned from lower mafic to upper evolved compositions and in which the melt fraction increased while the crystal size decreased toward the evolved top. This facilitated sampling of most of the vertical mush succession by the ascending mafic magma, which would have been highly fortuitous if different mush compositions were stored in spatially separate reservoirs. The glomerocrystic clasts do not show depletion of incompatible elements and enrichments of compatible elements that would be expected from significant crystal accumulation or melt extraction; they simply represent partially crystallized magmas that evolved along a common liquid line of descent marked by gradually increasing concentrations of Zr, Rb, Ba, etc., and decreasing concentrations of Sr, Ni, V, Sc etc. (Figs. 2, 3 and 4 and S4, S5) compatible with fractional crystallization; we did not find fractionated cumulates in our sample suite. Therefore, the glomerocrystic samples do not represent wall or floor crystal accumulations in the trachydacite reservoir, which fits the vertical separation of crystal-mush and trachydacite reservoirs discussed above. Since the time when an original trachydacitic melt escaped from the crystal mush, both the trachydacite and the crystal-mush had evolved further to rhyolitic melt compositions (except in the most mafic mush, Figs. 8 and 13b).

Before inflation of the glass matrix, the glomerocrystic clasts had mostly intersertal textures with impingement contacts between crystals (e.g., Fig. 6b). Most plagioclase crystals in a glomerocrystic clast share a narrow range in grain size as well as aspect ratio (long/short axis ~ 3–5), which indicates crystallization under a certain degree of undercooling over a limited time interval (Lofgren 1974; Holness 2014). The mafic and intermediate glomerocrystic clasts also contain a minor fraction of larger, tabular plagioclase crystals that are compositionally zoned, often include magnetite and olivine, and thus formed during early slow cooling. These textures all support crystallization unhindered by neighboring crystals in a melt-dominated environment rather than in a static highly crystallized mush (Holness et al. 2017, 2019). However, some mafic glomerocrystic fragments contain crystal clots of subophitic texture (typically clinopyroxene filling space between plagioclase crystals; e.g., Fig. 6h) or of intensely and densely intergrown crystals with smooth curved boundaries and dihedral angles. These textures indicate that some parts of the crystal mush body were approaching a holocrystalline state (possibly closer to reservoir walls) at the time of eruption.

Plagioclase with angular euhedral outer shapes but interior rounded, intensely resorbed zones occur in mafic to intermediate glomerocrystic clasts (JK003, JK049). Interior spots of An ~ 40 mol% compositions (Fig. 7a) may be relics of the original plagioclase (probably a xenocryst entrained from evolved plutonic wall rock) that was rounded by dissolution and intensely resorbed in a hotter magma (cf. Tsuchiyama 1985). Reactions between melt and plagioclase precipitated higher An ~ 60 mol% plagioclase, minor Or-rich ternary plagioclase, and a high-birefringence phase that is probably pyroxene (Fig. 7a). Subsequent normally-zoned overgrowth by equilibrium plagioclase rebuilt a euhedral crystal shape.

The Alpehué glomerocrystic clasts represent a crystal mush body with a wide compositional range but without evidence for large vertical extension through the crust as envisaged in some mush-zone models (e.g., Cashman et al. 2017; Sparks et al. 2019). We interpret it as an upper-crustal zoned magma chamber because we see no evidence for higher-pressure (lower-crustal) evolution. This magma reservoir evolved along a typical Sollipulli differentiation path but was not the direct source of the erupted Alpehué trachydacite magma. It may be a "left-over" of the magmatic system that produced the Sollipulli CC unit at 26 ± 5 ka (Lachowycz et al. 2015) and which was still active ~ 20.000 years later when the Alpehué tephra erupted. Murphy (1996) described a second population of crystals and crystal clots next to the major phenocryst population in the older Sollipulli rocks, which may be derived from that mushy reservoir but this requires further investigation.

Origin of the knobbly lava types

We have petrographically distinguished three types of knobbly lavas that differ by their crystal loads. Types 1 and 2 share the same phenocryst assemblage of plagioclase (An > 86 mol%), olivine (Fo > 79 mol%) and clinopyroxene but type 1 is phenocryst-poor while type 2 is rich in mostly large plagioclase and olivine phenocrysts which are almost unzoned and form large compact aggregates (Fig. 7c). The microcrystalline matrix in type 1 comprises plagioclase and amphibole with subordinate olivine while type 2 matrix has no amphibole. Amphibole in type-1 matrix precipitated when temperature had dropped below the amphibole stability limit at the trachydacite reservoir depth. Entrained glomerocrystic fragments do rarely occur as well as zoned low-An plagioclase (associated with orthopyroxene, i.e., entrained from the trachydacite) that has been marginally resorbed in type 1 (Fig. 7b) but not in type 2 samples.

Type 3 knobbly lavas are intensely mingled samples of amphibole-bearing and amphibole-free, olivine-bearing glomerocrystic material (Table S6) with microcrystalline lava in which original basaltic phenocrysts (if present at all) and mush-derived crystals are practically indistinguishable. Such mixing is probably the reason why type 3 knobbly lavas have more evolved bulk compositions (3.5–4.4 wt% MgO; Fig. S5) than type 1 and 2 lavas (5.12–5.43 wt% MgO). High-An plagioclase and high-Fo olivine occur as overgrown cores of crystals in the glomerocrystic fragments (Fig. 9) with no relation to the admixed mafic magma. Type 3 knobbly lava samples also contain plagioclase with angular euhedral outer shapes but interior rounded, intensely resorbed zones (JK075c, JK114) as in glomerocrystic clasts

(JK003, JK049; Fig. 7a) from which they are probably inherited. The basaltic magma that mingled with crystal mush to form type 3 compositions may have been type 1 magma or a third similarly phenocryst-poor mafic magma but it was not type 2 magma because the large unzoned plagioclase and olivine crystals do not occur in type 3 samples.

Thus, the magmatic activity precursory to the Alpehué eruption involved two or possibly three ascending basaltic to basaltic-andesitic magma batches which share a common petrogenesis (Figs. 2, 3 and 4). Type 1 represents near-liquidus magma with just few olivine and plagioclase phenocrysts while type 2 magma was thermally buffered for some time below olivine and plagioclase but above clinopyroxene liquidus to facilitate the growth of large homogeneous olivine and plagioclase phenocrysts and crystal clots. Knobbly lava samples free of admixed glomerocrystic components suggest that some of the ascending mafic magma penetrated the crystal-mush body without significant mixing (probably along the inside of a conduit or dike) while other mafic magma mixed intensely with disintegrated glomerocrystic material (probably along conduit margins) to form type 3. There is no petrographic evidence for significant thermal overprinting or melting even in the most evolved glomerocrystic clasts, which implies short residence time in the hot magma before eruption.

Entrainment and transport of glomerocrystic fragments

The melt fraction in the glomerocrystic clasts (Fig. 2c) was sufficient to form a connected network isolating crystals and crystal clots even before vesiculation which facilitated disintegration and entrainment by penetrating mafic magma without the need for brittle fracturing. Heating of entrained crystal-mush fragments caused viscosity reduction and thermal expansion of the interstitial melt, facilitating further disintegration.

The matrix glasses of intermediate and evolved glomerocrystic clasts share very similar rhyolitic compositions (Figs. 8 and 13b). The presence of amphibole and the hygrometrically determined ~ 5 wt% dissolved H_2O (Fig. 12) suggest that at least the evolved upper part of the zoned crystal-mush reservoir may have reached water saturation at ~ 150 MPa at the time of the Alpehué eruption (Fig. 13a). When fragments of such saturated mush get heated by entrainment into hot basaltic magma, the negative temperature dependence of water solubility (Fig. 13a; Lavallee et al. 2015; Burchardt et al. 2016; Berg et al. 2016) would cause vesiculation. For example, using the water solubility function for rhyolitic melt of Liu et al. (2005) and assuming equilibrium vesiculation, heating by 50° would result in 0.5–1 vol% vesicles at 200 – 100 MPa pressure which may have forced further disintegration of entrained crystal-mush fragments, particularly with immediately following expansion during decompression. At its storage pressure of ~ 100 MPa the rhyolitic melt of the trachydacite magma had also reached water saturation with around 4 wt% dissolved H_2O (Fig. 13a). However, in the course of ascent and eruption, the evolved and intermediate crystal mush fragments have a significant lead of ~ 10 vol% in vesicularity which they keep until fragmentation (Fig. 14a). This is actually observed in the erupted glomerocrystic fragments (Fig. 6a) which *a posteriori* supports their higher saturation pressure. The commonly observed in-situ fragmentation of (typically elongated) crystals and crystal clots and the presence of angular crystal fragments in the glomerocrystic clasts (Fig. 6b) probably resulted from the significant tensile stress exerted by vesiculation in the viscous rhyolitic melt during ascent.

The vesicular matrix glass in most mafic glomerocrystic inclusions in type-3 knobbly lavas contains amphibole and plagioclase skeletal crystals (Fig. 6g, typically needle, hopper or fan shapes) indicating high degrees of undercooling (Lofgren 1974; Donaldson 1985; Coombs et al. 2002). The enigmatic quenched-matrix rims around vesicles in type-2 knobbly lava (Fig. 6e, f) are very similar to the matrix in mafic glomerocrystic clasts. The rims are composed of skeletal, needle-shaped crystals of low-An plagioclase and low-Mg# amphibole as well as high-silica glass (C169 in Figs. 8, 9 and 11), while the surrounding basaltic microcrystalline matrix is composed of tabular to lath-shaped plagioclase with minor pyroxene and olivine. We found no phenocrysts intergrown with the rims of these vesicles; however, one of such rimmed vesicles occurs inside a larger, internally hollow An ~60 mol% plagioclase distinct from the An ~ 80 mol% basaltic phenocrysts. We interpret the rimmed vesicles as entrained drops of interstitial melt from mafic crystal mush. The quench crystallization in these drops as well as in the glomerocrystic fragments was not caused by rapid decompression during eruption because this occurs at pressures too low to stabilize amphibole, where amphibole is not precipitated even under disequilibrium crystallization conditions (Shea and Hammer 2013). Large vesicle size and large vesicle/matrix volume ratio of the rimmed vesicles, and the much higher vesicularity of the glass in the glomerocrystic clasts, suggest that this melt was more water-rich and degassed earlier than the host basalt magma (which partly degassed upon cooling in the trachydacite reservoir). Therefore, we attribute partial quench crystallization in the mafic glomerocrystic material to decompression-degassing during ascent toward the trachydacite reservoir. The round shape of the vesicles indicates that they grew unhindered by basalt matrix strength, i.e., before the basaltic magma itself got quenched in the trachydacite reservoir.

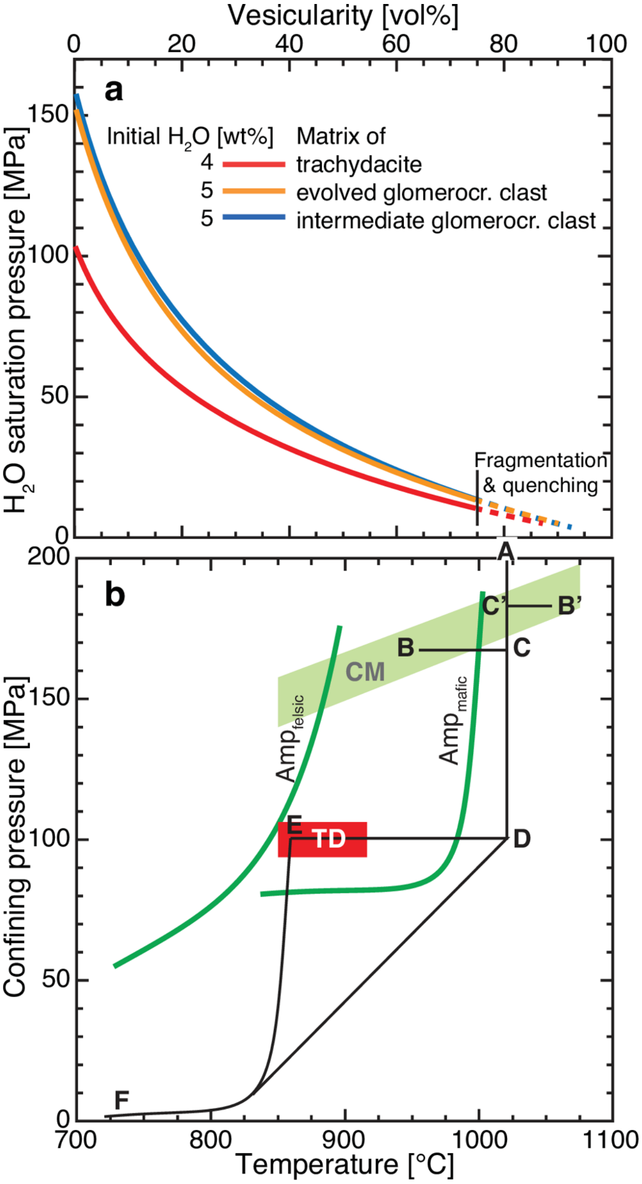

Fig. 14 (a) Below the respective saturation pressure calculated after Liu et al. (2005), the vesicularity increase towards lower pressure is determined assuming equilibrium vesiculation. More hydrous intermediate to evolved crystal mush fragments would have an ~ 10 vol% lead on the vesicularity of trachydacite pumice. (b) Qualitative illustration of the relationships between amphibole phase boundaries (different for mafic and felsic magmas) and magma ascent paths as discussed in the text. TD and CM mark the trachydacite and crystal-mush reservoirs, respectively

Intrusion and disintegration of mafic magma

Some of the knobbly lava clasts have fracture surfaces probably formed by explosive fragmentation during eruption but the common knobbly surfaces are quenched clast margins that are darker and finer crystallized than the clast interiors. Such pillow-like shapes are formed when fluid basaltic magma gets immersed into relatively cool magma (e.g., Chapman 1962; Wiebe 1973, 2016) where clast formation and deformation must occur before a chilled margin becomes too thick for further deformation (Blake and Fink 2000). Quenching of the lava clasts occurred after the entrainment of crystals from the trachydacite magma but preserved a low (higher-pressure) vesicularity and most likely happened inside the trachydacite reservoir. However, some basaltic melt escaped early quenching such as the highly vesicular sideromelane associated with olivine in banded pumice JK068 (see above). The conductive cooling of mafic magma blebs (initially 1100 °C) typically < 10 cm in size to the basalt solidus (950 °C) in ambient trachydacite magma (850 °C) only requires a few hours at most.

However, sieve- or fingerprint-textured resorption zones (Fig. 7b) on xenocrysts entrained from the trachydacite (because unaltered cores match core compositions (Fig. 9) in pumice samples) challenge immediate rapid cooling after intrusion. Donaldson (1985) has determined dissolution rates of plagioclase crystals (An = 30 and 60 mol%) in basaltic melt at 1210–1300 °C. We apply an exponential fit to his data to estimate dissolution rates at the lower temperatures (1000–1100 °C) relevant here and obtain 210–630 µm/day and 40–210 µm/day, respectively. Note that these rates are for simple dissolution whereas resorption involves both dissolution and new precipitation (Stewart and Pearce 2004). However, at such rates the up to 400 µm thick fingerprint zones of An ~30–50 mol% plagioclase crystals in the knobbly lava would have needed at least < 1 to 10 days to develop. Therefore, disintegration of basaltic magma by rapid intrusion and fountaining (Campbell and Turner 1986, 1989) followed by almost immediate quenching is unlikely. More likely, basaltic magma intruded in lava-like (cf. Wiebe and Snyder 1993) or dike-like fashion (cf. Andrews and Manga 2014; Rooyakkers et al. 2018) with only minor mixing leading to plagioclase entrainment (e.g., into a fingering flow front; Snyder and Tait 1995). Such mixing was very limited because knobbly lava chemical compositions give no indication of bulk mixing with trachydacite.

The calculated resorption times provide a minimum residence time between intrusion and eruption for types 1 and 3 knobbly lavas; type 2 knobbly lava contains entrained plagioclase that is not resorbed and thus requires a shorter residence time if any. The matrix texture and composition differ between types 1 and 2 with amphibole-rich type 1 matrix (Fig. 6d) about two times coarser than amphibole-free clinopyroxene-bearing type 2 matrix (Fig. 6e, f), and matrix plagioclase is more elongated and slightly more calcic in type-1 than in type-2 matrix (Fig. 9). By comparison with experiments of Shea and Hammer (2013) these observations imply higher degrees of undercooling for type-1 than for type-2 melt.

All knobbly lava magmas ascended at temperatures above amphibole stability (path A-D in Fig. 14b) because amphibole phenocrysts are absent (assuming that apparent amphibole phenocrysts in type-3 samples are all crystal mush-derived). Glomerocrystic fragments bearing amphibole phenocrysts were entrained along paths such as B-C (Fig. 14b) crossing the amphibole stability limit as they were heated in the host mafic magma but total transport time of these fragments until eruption and quenching at Earth's surface was too short for any breakdown reactions. According to the experiments of Rutherford and Hill (1993) this requires average decompression rate >25 MPa/day, or <6 days from entrainment (B-C) to quenching (E-F) (which fits the estimate from faster plagioclase resorption). As a note of caution, it appears that amphibole reactions were much slower in experiments of Hammer and Rutherford (2003).

Type-1 knobbly lava samples have amphibole next to plagioclase in their microcrystalline matrix. This magma entered the trachydacite reservoir, cooled towards the ambient temperature and thereby crossed into the amphibole stability field (path D-E in Fig. 14b). On the other hand, type-2 samples, the lava region in type-3 sample JK075b, and the most mafic glomerocrystic clast JK003 do not have amphibole in their microcrystalline assemblage. Entrainment of JK003 into the ascending mafic magma along a path like B'-C' (Fig. 14b) may have involved minor cooling (cf. Table 1) but did not reach the amphibole boundary. These amphibole-free magma batches contained sufficient water for amphibole precipitation but must have followed a path of cooling and decompression crystallization that remained outside the amphibole stability field (D-F in Fig. 14b). This means that, although they physically passed through the trachydacite reservoir, their cooling occurred shortly before or even during eruption so that they never entered the amphibole stability conditions.

All knobbly lava samples are poorly vesicular and the thermohygrometric data suggest 2–4 wt% dissolved H_2O at the time of early plagioclase precipitation which would not allow for vesiculation at pressures >100 MPa (Fig. 13a). In type-1 samples microlite growth into irregular vesicles (Fig. 6d) suggests contemporaneous cooling-driven matrix crystallization and vesiculation by second boiling probably within the trachydacite reservoir but increasing solidification stopped vesiculation at low porosity values. The very low porosity of type-2 knobbly lava clasts indicates an even earlier interruption of the vesiculation process.

In summary, type-1 basalt magma appears to have intruded the trachydacite reservoir first, possibly a few days before eruption, entrained and resorbed some plagioclase from the host magma, and was ultimately fragmented and quenched. Type-2 basalt magma penetrated the trachydacite reservoir shortly before or during eruption without significant residence because entrained plagioclase was not resorbed and matrix amphibole did not precipitate. The ascent history of type-3 magma is probably similar to type-1 but entrainment of crystal-mush material can have affected its cooling and crystallization history.

Eruption trigger

The presence of mafic, apparently comagmatic inclusions in the Alpehué tephra suggests mafic replenishment of the trachydacite reservoir as a plausible eruption trigger (Naranjo et al. 1993), a scenario for which Cassidy et al. (2018) have reviewed a number of possible processes. We do, however, not find evidence for a massive overturn of highly vesiculated mafic magma (Eichelberger 1980) or for extensive heating and convection of the felsic magma (Sparks et al. 1977). Our results suggest that eruption triggering by mafic magma injection involved several steps:

(1) Earlier heating events, most likely caused by mafic intrusions and demonstrated by resorption and discontinuous zonation patterns of plagioclase phenocrysts of the trachydacite (Fig. 5), did not cause eruption.

(2) The mafic magmas represented by the knobbly lava samples invaded the trachydacite reservoir in at least two separate pulses (Fig. 13b): first type 1 with subsequent resorption of entrained plagioclase, later type 2 without such resorption shortly before eruption.

(3) At the time of eruption, the resident trachydacite had most likely reached water saturation and was thus critically susceptible to disturbances. Type-1 magma intrusion did not immediately trigger the eruption but type-2 magma intrusion finally succeeded in driving reservoir pressure above eruption threshold. The evolved upper part of the underlying crystal mush reservoir apparently had also reached water saturation and we speculate that escaping fluids (e.g., Parmigiani et al. 2017) may have entered the trachydacite reservoir.

Once triggered, the eruption succeeded in almost immediately stabilizing a high-discharge rate Plinian eruption column as evidenced by the rapid increase in grain size at the base of the fallout tephra (see supplement S1). A favorable condition may also have been the presence of a conduit that had already been created by extrusion of minor crystal-poor melt from the top of the reservoir which had lost its gas phase during passage through a permeable conduit (Eichelberger et al. 1986) and formed an obsidian (crypto-)dome at the surface, the source of the co-magmatic obsidian fragments (O1 in Figs. 2, 3 and 4) in the Alpehué tephra.

Conclusions

The Alpehué tephra is composed of crystal-rich (up to ~30 vol%) trachydacitic pumice and ash but includes additional minor comagmatic components: (1) comagmatic (but also xenolithic) obsidian fragments, (2) highly inflated glomerocrystic clasts with high crystal-glass ratios (~1 to 3) which range from basaltic to trachytic compositions, and (3) quenched knobbly lava fragments, which we divide into three types. Type-1 knobbly lava samples are phenocryst-poor basalt, type 2 basalt contains abundant large, unzoned olivine and plagioclase crystals and crystal clots, and type 3 represents intense mixtures between poorly phyric basalt and crystal mush-derived material.

All comagmatic components form a coherent, continuous differentiation path in major and trace element geochemical diagrams that overlaps with that formed by older Sollipulli rocks. In particular, the glomerocrystic clasts show no sign of incompatible element depletion or compatible element enrichment that would indicate significant crystal-melt segregation. We interpret these samples to represent a crystal-mush magma chamber continuously zoned from basal basaltic (~1100 °C, ~70% crystals) to upper trachytic (~850 °C, ~40% crystals) bulk-rock composition. Amphibole is a stable phenocryst phase (and has partly replaced clinopyroxene) throughout this reservoir except for the hottest, most mafic basal part.

In contrast, the main trachydacite does not contain amphibole phenocrysts although plagioclase-melt hygrometry yields water contents around 4 wt% H_2O. The depth of the trachydacite reservoir (at ~850 °C) is therefore constrained (a) by a minimum pressure of ~100 MPa in order to avoid significant water oversaturation (Figs. 12 and 13a), and (b) by a maximum pressure not much greater than 100 MPa in order to remain outside the amphibole stability field (Fig. 13a). This implies that the trachydacite reservoir formed a shallower, separate magma body and was not part of the crystal-mush reservoir which resided inside amphibole stability conditions at around 150–200 MPa as estimated from calculated water contents, barometric results and volume considerations.

The main trachydacite has large zoned plagioclase as its predominant phenocryst phase next to clinopyroxene and orthopyroxene which crystallized sequentially and not in equilibrium. Plagioclase zonations comprise a patchy resorbed core with variable An contents that is overgrown by finely stratified zonation through which An contents decrease outward but in an unsteady, zig-zag fashion with minor unconformities in stratification and with interruption by a major resorption zone rich in melt inclusions. This demonstrates a long history of differentiation of the trachydacite magma towards its rhyolitic melt composition that was repeatedly disturbed by heating events probably associated with mafic-magma underplating.

However, only the ascent of the at least two mafic magmas forming the knobbly lava fragments succeeded in triggering the eruption, probably because the trachydacite had finally reached a state of water (over-)saturation. These rising basaltic magmas passed through the crystal-mush reservoir and entrained samples from its complete compositional range. The presence of melt, heating in the hot host magma and vesiculation promoted disintegration of the crystal-mush material. The absence of any breakdown reactions in glomerocrystic amphibole and the width of fingerprint-resorption rims on trachydacite-derived plagioclase in type-1 knobbly lava constrain the duration of ascent and residence until eruption to a few days but type-2 basalt only intruded immediately before or during eruption.

The presence of crystal-rich fragments such as the glomerocrystic clasts in the Alpehué tephra is generally taken as evidence for the presence of a crystal-mush reservoir. There is no evidence that Sollipulli caldera was ever associated with a large-volume evolved magma reservoir (Gilbert et al. 1996), the Alpehué tephra erupted from a moderate-volume magma chamber (~8 km^3 tephra volume, Naranjo et al. 1993), and our investigation yielded magma evolution constrained to the upper crust. The Sollipulli crystal mush body was thus a reservoir of moderate volume that did not extend through the entire crust as advocated for large-volume silicic systems (e.g., Cashman et al. 2017; Sparks et al. 2019). The Sollipulli crystal mush most likely was the source of a "parental" Alpehué trachydacite melt but its extraction from the mush must have occurred a long time before the eruption (a) because of the subsequent complex evolution of the trachydacite as recorded in zoned plagioclase and (b) because ~3000 years ago the mush melt had already become rhyolitic (except in the most mafic part).

Supplementary Information The online version contains supplementary material available at https://doi.org/10.1007/s00410-024-02195-0.

Acknowledgements This paper extends work begun with the diploma thesis of K. Strehlow (2012). This publication is a contribution of the Sonderforschungsbereich 574 "Volatiles and Fluids in Subduction Zones" at Kiel University. We thank S. Jung (University of Hamburg) and M. Thöner (GEOMAR Helmholtz Centre for Ocean Research Kiel) for their support with XRF and EMP analyses, respectively. We are also grateful for the support of our field work particularly by L. Lara, J. Naranjo (Servicio Nacional de Geología y Minería, Santiago, Chile) and P. Sruoga (CONICET-SEGEMAR, Buenos Aires, Argentina). Constructive reviews by E. First and P. Alasino as well as comments by O. Müntener helped much to improve this paper.

Funding Open Access funding enabled and organized by Projekt DEAL.

References

Allan ASR, Barker SJ, Millet MA, Morgan DJ, Rooyakkers SM, Schipper CI, Wilson CJN (2017) A cascade of magmatic events during the assembly and eruption of a super–sized magma body. Contrib Mineral Petrol 172:49. https://doi.org/10.1007/s00410-017-1367-8

Almeev RR, Holtz F, Koepke J, Parat F (2012) Experimental calibration of the effect of H_2O on plagioclase crystallization in basaltic melt at 200 MPa. Am Min 97:1234–1240

Andersen DJ, Lindsley DH (1985) New (and final!) Models for the Ti-magnetite/ilmenite geothermometer and oxygen barometer. EOS Trans Am Geophys Union 66:416

Andrews BJ, Manga M (2014) Thermal and rheological controls on the formation of mafic enclaves or banded pumice. Contrib Mineral Petrol 167:961. https://doi.org/10.1007/s00410-013-0961-7

Bachmann O, Bergantz GW (2004) On the origin of crystal-poor rhyolites: extracted from batholithic crystal mushes. J Petrol 45:1565–1582

Bachmann O, Bergantz GW (2008) Rhyolites and their source mushes across tectonic settings. J Petrol 49:2277–2285. https://doi.org/10.1093/Petrology/Egn068

Bacon CR, Hirschmann MM (1988) Mg/Mn partitioning as a test for equilibrium between coexisting Fe-Ti oxides. Am Mineral 73:57–61

Barclay J, Carmichael ISE (2004) A hornblende basalt from western Mexico: Water-saturated phase relations constrain a pressure-temperature window of eruptability. J Petrol 45:485–506. https://doi.org/10.1093/petrology/egg091

Bedard JH (2006) Trace element partitioning in plagioclase feldspar. Geochim Cosmochim Acta 70(14):3717–3742. https://doi.org/10.1016/j.gca.2006.05.003

Bedard JH (2023) Trace element partitioning coefficients between terrestrial silicate melts and plagioclase feldspar: Improved and simplified parameters. Geochim Cosmochim Acta 350:69–86. https://doi.org/10.1016/j.gca.2023.04.010

Bennett EN, Lissenberg CJ, Cashman KV (2019) The significance of plagioclase textures in mid–ocean ridge basalt (Gakkel Ridge, Arctic Ocean). Contrib Mineral Petrol 174:49. https://doi.org/10.1007/s00410-019-1587-1

Berg SE, Troll VR, Deegan FM, Burchardt S, Krumbholz M, Mancini L, Polacci M, Carracedo JC, Soler V, Arzilli F, Brun F (2016) Heterogeneous vesiculation of 2011 El Hierro xeno-pumice revealed by X-ray computed microtomography. Bull Volcanol 78:85. https://doi.org/10.1007/s00445-016-1080-x

Berndt J, Koepke J, Holtz F (2005) An experimental investigation of the influence of water and oxygen fugacity on differentiation of MORB at 200 MPa. J Petrol 46:135–167

Blake S, Fink JH (2000) On the deformation and freezing of enclaves during magma mixing. J Volcanol Geotherm Res 95:1–8

Bowen NL (1928) The evolution of the igneous rocks. Princeton University Press, London, UK: p. 332 (reprint 1956, Dover Publications, New York)

Burchardt S, Troll VR, Schmeling H, Koyi H, Blythe L (2016) Erupted frothy xenoliths may explain lack of country-rock fragments in plutons. Sci Rep 6:34566. https://doi.org/10.1038/srep34566

Campbell IH, Turner JS (1986) The influence of viscosity on fountains in magma chambers. J Petrol 27:1–30

Campbell IH, Turner JS (1989) Fountains in magma chambers. J Petrol 30:885–923

Cashman KV, Sparks RSJ, Blundy JD (2017) Vertically extensive and unstable magmatic systems: a unified view of igneous processes. Science 355:1280. https://doi.org/10.1126/science.aag3055

Cassidy M, Manga M, Cashman K, Bachmann O (2018) Controls on explosive-effusive volcanic eruption styles. Nat Communications 9:2839. https://doi.org/10.1038/s41467-018-05293-3

Chapman CA (1962) Diabase - granite composite dikes, with pillow-like structure, Mount Desert Island, Maine. J Geol 70:539–564

Cisneros de Leon A, Schmitt A, Kutterolf S, Schindlbeck-Belo JC, Hernandez W, Sims K, Garrison J, Kant L, Weber B, Wang KL (2021) Zircon and melt extraction from a long-lived and vertically extensive magma system underneath Ilopango Caldera (El Salvador). G-cubed 22, e2020GC009507

Claiborne LL, Miller CF, Flanagan DM, Clynne MA, Wooden JL (2010) Zircon reveals protracted magma storage and recycling beneath Mount St. Helens Geol 38(11):1011–1014. https://doi.org/10.1130/G31285.1

Coombs ML, Eichelberger JC, Rutherford MJ (2002) Experimental and textural constraints on mafic enclave formation in volcanic rocks. J Volcanol Geotherm Res 119:125–144

Cooper KM (2019) Time scales and temperatures of crystal storage in magma reservoirs: implications for magma reservoir dynamics. Phil Trans R Soc A 377:20180009. https://doi.org/10.1098/rsta.2018.0009

Cooper GF, Wilson CJN (2014) Development, mobilisation and eruption of a large crystal-rich rhyolite: the Ongatiti Ignimbrite, New Zealand. Lithos 198–199:38–57. https://doi.org/10.1016/j.lithos.2014.03.014

Cooper GF, Blundy JD, Macpherson CG, Humphreys MCS, Davidson JP (2019) Evidence from plutonic xenoliths for magma differentiation, mixing and storage in a volatile–rich crystal mush beneath St. Eustatius, Lesser Antilles. Contrib Mineral Petrol 174:39. https://doi.org/10.1007/s00410-019-1576-4

Costa F, Scaillet B, Pichavant M (2004) Petrological and experimental constraints on the pre-eruption conditions of Holocene dacite from Volcan San Pedro (36°S, Chilean Andes) and the importance of sulphur in silicic subduction-related magmas. J Petrol 45:855–881

Costa F, Dohmen R, Chakraborty S (2008) Time scales of magmatic processes from modeling the zoning patterns of crystals. In: Putirka KD, Tepley FJ III (eds) Minerals, inclusions and volcanic processes . Rev Mineral Geochem 69:333–362

Degruyter W, Parmigiani A, Huber C, Bachmann O (2019) How do volatiles escape their shallow magmatic hearth? Phil Trans R Soc A377:20180017. https://doi.org/10.1098/rsta.2018.0017

Donaldson CH (1985) The rates of dissolution of olivine, plagioclase, and quartz in a basalt melt. Mineral Mag 49:683–693. https://doi.org/10.1180/minmag.1985.049.354.07

Druitt TH, Costa F, Deloule E, Dungan M, Scaillet B (2012) Decadal to monthly timescales of magma transfer and reservoir growth at a caldera volcano. Nature 482:77–80. https://doi.org/10.1038/nature10706

Eichelberger JC (1980) Vesiculation of mafic magma during replenishment of silicic magma reservoirs. Nature 288:446–450

Eichelberger JC, Carrigan CR, Westrich HR, Price RH (1986) Non-explosive silicic volcanism. Nature 323:598–602

Farr TG, Rosen PA, Caro E, Crippen R, Duren R, Hensley S, Kobrick M, Paller M, Rodriguez E, Roth L, Seal D, Shaffer S, Shimada J, Umland J, Werner M, Oskin M, Burbank D, Alsdorf D (2007) The shuttle radar topography mission. Rev Geophys 45:1–33

Feig ST, Koepke J, Snow JE (2006) Effect of water on tholeiitic basalt phase equilibria: an experimental study under oxidizing conditions. Contrib Mineral Petrol 152:611–638

First EC, Hammer JE, Ruprecht P, Rutherford M (2021) Experimental constraints on Dacite Magma Storage beneath Volcan Quizapu, Chile. J Petrol 2021:1–26. https://doi.org/10.1093/petrology/egab027

Garbe-Schönberg C-D (1993) Simultaneous determination of thirty-seven trace elements in twenty-eight international rock standarts by ICP-MS. Geostandard Newsl 17(1):81–97

Gilbert JS, Stasiuk MV, Lane SJ, Adam CR, Murphy MD, Sparks RSJ, Naranjo JA (1996) Non-explosive, constructional evolution of the ice-filled caldera at Volcán Sollipulli, Chile. Bull Volcanol 58:67–83

Ginibre C, Kronz A, Wörner G (2002) High-resolution quantitative imaging of plagioclase composition using accumulated backscattered electron images: new constraints on oscillatory zoning. Contrib Mineral Petrol 142:436–448

Hammer JE, Rutherford MJ (2003) Petrologic indicators of preeruption magma dynamics. Geology 31(1):79–82. https://doi.org/10.1130/0091-7613(2003)031-0079:PIOPMD-2.0.CO;2

Hammer JE, Rutherford MJ, Hildreth W (2002) Magma storage prior to the 1912 eruption at Novarupta, Alaska. Contrib Mineral Petrol 144:144–162

Hawkesworth CJ, Blake S, Evans P, Hughes R, Macdonald R, Thomas LE, Turner SP, Zellmer G (2000) Time scales of crystal fractionation in magma chambers – integrating physical, isotopic and geochemical perspectives. J Petrol 41:991–1006

Hildreth W, Wilson CJN (2007) Compositional zoning of the bishop tuff. J Petrol 48:951–999. https://doi.org/10.1093/petrology/egm007

Holness MB (2014) The effect of crystallization time on plagioclase grain shape in dolerites. Contrib Mineral Petrol 168:1076. https://doi.org/10.1007/s00410-014-1076-5

Holness MB, Vukmanovic Z, Mariani E (2017) Assessing the role of Compaction in the formation of adcumulates: a Microstructural Perspective. J Petrol 58(4):643–674. https://doi.org/10.1093/petrology/egx037

Holness MB, Stock MJ, Geist D (2019) Magma chambers versus mush zones: constraining the architecture of sub-volcanic plumbing systems from microstructural analysis of crystalline enclaves. Phil Trans R Soc A377:20180006. https://doi.org/10.1098/rsta.2018.0006

Holtz F, Sato H, Lewis J, Behrens H, Nakada S (2005) Experimental petrology of the 1991–1995 Unzen dacite, Japan. Part I: phase relations, phase compositions and pre-eruptive conditions. J Petrol 46:319–337

Holtzman BK, Groebner NJ, Zimmerman ME, Ginsberg SB, Kohlstedt DL (2003) Stress-driven melt segregation in partially molten rocks. Geochem Geophys Geosyst 4(5):8607. https://doi.org/10.1029/2001GC000258

Humphreys MCS, Blundy JD, Sparks RSJ (2006) Magma evolution and open-system processes at Shiveluch volcano: insights from phenocryst zoning. J Petrol 47(12):2303–2334. https://doi.org/10.1093/petrology/egl045

Huppert HE, Sparks RSJ (1984) Double-diffusive convection due to crystallization in magmas. Ann Rev Earth Planet Sci 12:11–37

Johannes W (1989) Melting of plagioclase-quartz assemblages at 2 kbar water pressure. Contrib Mineral Petrol 103:270–276

Kuo LC, Kirkpatrick RJ (1982) Pre-eruption history of phyric basalts from DSDP Legs 45 and 46: evidence from morphology and zoning patterns in plagioclase. Contrib Mineral Petrol 79:13–27

Kutterolf S, Freundt A, Burkert C (2011) Eruptive history and magmatic evolution of the 1.9 Kyr Plinian Dacitic Chiltepe Tephra from Apoyeque volcano in west-central Nicaragua. Bull Volcanol 73(7):811–831

Lachowycz SM, Pyle DM, Gilbert JS, Mather TA, Mee K, Naranjo JA, Hobbs LK (2015) Glaciovolcanism at Volcán Sollipulli, southern Chile: Lithofacies analysis and interpretation. J Volcanol Geotherm Res 303:59–78

Lavallee Y, Dingwell DB, Johnson JB, Cimarelli C, Hornby AJ, Kendrick JE, von Aulock FW, Kennedy BM, Andrews BJ, Wadsworth FB, Rhodes E, Chigna G (2015) Thermal vesiculation during volcanic eruptions. Nature 528:544–547. https://doi.org/10.1038/nature16153

Le Maitre RW, Bateman P, Dudek A, Keller J, Lameyre J, Le Bas MJ, Sabine PA, Schmid R, Sorensen H, Streckeisen A, Woolley AR, Zanettin B (1989) A classification of igneous rocks and glossary of terms. Blackwell Scientific Publ., Oxford - London - Edinburgh - Boston - Melbourne, pp 1–193

Lepage LD (2003) ILMAT: an Excel worksheet for ilmenite–magnetite geothermometry and geobarometry. Comput Geosci 29:673–678

Liu Y, Zhang Y, Behrens H (2005) Solubility of H_2O in rhyolitic melts at low pressures and a new empirical model for mixed H_2O-CO_2 solubility in rhyolitic melts. J Volcanol Geotherm Res 143:219–235

Lofgren GE (1974) An experimental study of plagioclase crystal morphology: isothermal crystallization. Am J Sci 274:243–273. https://doi.org/10.2475/ajs.274.3.243

Marsh BD (1989) Magma chambers. Ann Rev Earth Planet Sci 17:439–474

Martin D, Nokes R (1988) Crystal settling in a vigorously convecting magma chamber. Nature 332:534–536

McBirney AR, Noyes RM (1979) Crystallization and layering of the Skaergaard intrusion. J Petrol 20:487–554

Melekhova E, Blundy J, Martin R, Arculus R, Pichavant M (2017) Petrological and experimental evidence for differentiation of water–rich magmas beneath St. Kitts, Lesser Antilles. Contrib Mineral Petrol 172:98. https://doi.org/10.1007/s00410-017-1416-3

Molina JF, Moreno JA, Castro A, Rodríguez C, Fershtater GB (2015) Calcic amphibole thermobarometry in metamorphic and igneous rocks: New calibrations based on plagioclase/amphibole Al-Si partitioning and amphibole/liquid mg partitioning. Lithos 232:286–305. https://doi.org/10.1016/j.lithos.2015.06.027

Moore G, Carmichael ISE (1998) The hydrous phase equilibria (to 3 kbar) of an andesite and basaltic andesite from western Mexico: constraints on water content and conditions of phenocryst growth. Contrib Mineral Petrol 130:304–319

Moore G, Vennemann T, Carmichael ISE (1998) An empirical model for the solubility of H_2O in magmas to 3 kilobars. Am Mineral 83:36–42

Murphy MD (1996) Magmatic evolution at Volcan Sollipulli, southern Andes of Chile. PhD thesis, University of Bristol, UK, p 304

Mutch EJF, Blundy JD, Tattitch BC, Cooper FJ, Brooker RA (2016) An experimental study of amphibole stability in low–pressure granitic magmas and a revised Al–in–hornblende geobarometer. Contrib Mineral Petrol 171:85. https://doi.org/10.1007/s00410-016-1298-9

Naranjo JA, Moreno H, Emparan C, Murphy M (1993) Volcanismo explosivo reciente en la caldera del volcán Sollipulli, Andes Del Sur (39°S). Revista Geológica De Chile 20:167–191

Nelson ST, Montana A (1992) Sieve-textured plagioclase in volcanic rocks produced by rapid decompression. Am Mineral 77:1242–1249

Parmigiani A, Degruyter W, Leclaire S, Huber C, Bachmann O (2017) The mechanics of shallow magma reservoir outgassing. Geochem Geophys Geosyst 18:2887–2905. https://doi.org/10.1002/2017GC006912

Pietranik A, Koepke J, Puziewicz J (2006) Crystallization and resorption in plutonic plagioclase: implications on the evolution of granodiorite magma (Gęsiniec Granodiorite, Strzelin Crystalline Massif, SW Poland). Lithos 86(3–4):260–280. https://doi.org/10.1016/j.lithos.2005.05.008

Polacci M, Papale P, Rosi M (2001) Textural heterogeneities in pumices from the climactic eruption of Mount Pinatubo, 15 June 1991, and implications for magma ascent dynamics. Bull Volcanol 63:83–97

Putirka KD (2008) Thermometers and barometers for volcanic systems. In: Putirka KD, Tepley FJ III (eds) Minerals, inclusions and volcanic processes, Rev Mineral Geochem 69: 61–120

Putirka KD (2016) Amphibole thermometers and barometers for igneous systems, and some implications for eruption mechanisms of felsic magmas at arc volcanoes. Am Mineral 101:841–858. https://doi.org/10.2138/am-2016-5506

Ridolfi F, Renzulli A (2012) Calcic amphiboles in calc-alkaline and alkaline magmas: thermobarometric and chemometric empirical equations valid up to 1,130°C and 2.2 GPa. Contrib Mineral Petrol 163:877–895. https://doi.org/10.1007/s00410-011-0704-6

Righter K, Carmichael ISE (1996) Phase equilibria of phlogopite lamprophyres from western Mexico: biotite-liquid equilibria and P-T estimates for biotite-bearing igneous rocks. Contrib Mineral Petrol 123:1–21

Rivera A, Bown F (2013) Recent glacier variations on active ice capped volcanoes in the Southern Volcanic Zone (37°–46°S), Chilean Andes. J South Am Earth Sci 45:345–356. https://doi.org/10.1016/j.jsames.2013.02.004

Roeder PL, Emslie RF (1970) Olivine-liquid equilibrium. Contrib Mineral Petrol 29:275–289

Rooyakkers SM, Wilson CJN, Schipper CI, Barker SJ, Allan ASR (2018) Textural and micro-analytical insights into mafic–felsic interactions during the Oruanui eruption, Taupo. Contrib Mineral Petrol 173:35. https://doi.org/10.1007/s00410-018-1461-6

Rutherford MJ, Hill PM (1993) Magma ascent rates from amphibole breakdown: an experimental study applied to the 1980–1986 Mount St. Helens eruptions. J Geophys Res 98:19667–19685

Sato H (1984) Partition coefficient of K between magma and plagioclase in a suite of volcanic rocks from northeast Shikoku, Japan. J Japan Assoc Min Petr Econ Geol 79:47–59

Sato H, Nakada S, Fujii T, Nakamura M, Suzuki-Kamata K (1999) Groundmass pargasite in the 1991–1995 dacite of Unzen volcano: phase stability experiments and volcanological implications. J Volcanol Geotherm Res 89:197–212

Scaillet B, Evans BW (1999) The 15 June 1991 eruption of Mount Pinatubo. I. Phase Equilibria and pre-eruption P-T-fO_2-fH_2O conditions of the dacitic magma. J Petrol 40:381–411

Seaman SJ, Chapman M (2008) The fate of basaltic enclaves during pyroclastic eruptions: an origin of andesitic ignimbrites. J Volcanol Geotherm Res 178:671–682

Shea T, Hammer JE (2013) Kinetics of cooling- and decompression-induced crystallization in hydrous mafic-intermediate magmas. J Volcanol Geotherm Res 260:127–145. https://doi.org/10.1016/j.jvolgeores.2013.04.018

Sielfeld G, Lange D, Cembrano J (2019) Intra-arc Crustal Seismicity: Seismotectonic implications for the Southern Andes Volcanic Zone, Chile. Tectonics 38:552–578. https://doi.org/10.1029/2018TC004985

Snyder D, Tait S (1995) Replenishment of magma chambers: comparison of fluid-mechanic experiments with field relations. Contrib Mineral Petrol 122:230–240

Solaro C, Martel C, Champallier R, Boudon G, Balcone-Boissard H, Pichavant M (2019) Petrological and experimental constraints on magma storage for large pumiceous eruptions in Dominica island (Lesser Antilles). Bull Volcanol 81:55. https://doi.org/10.1007/s00445-019-1313-x

Sparks RSJ, Sigurdsson H, Wilson L (1977) Magma mixing: a mechanism for triggering acid explosive eruptions. Nature 267:315–318

Sparks RSJ, Annen C, Blundy JD, Cashman KV, Rust AC, Jackson MD (2019) Formation and dynamics of magma reservoirs. Phil Trans R Soc A 377:20180019. https://doi.org/10.1098/rsta.2018.0019

Stewart ML, Pearce TH (2004) Sieve-textured plagioclase in dacitic magma: interference imaging results. Am Mineral 89(2–3):348–351. https://doi.org/10.2138/am-2004-2-313

Stormer JC (1983) The effects of recalculation on the estimates of temperature and oxygen fugacity from analyses of multicomponent iron-titanium oxides. Am Mineral 68:586–594

Strehlow K (2012) Magmatic evolution and eruption history of the 2900 years old Plinian Alpehue Tephra, Sollipulli caldera, southern Chile. Diploma thesis, Christian-Albrechts University, Kiel, Germany: p. 276

Sun C, Graff M, Liang Y (2017) Trace element partitioning between plagioclase and silicate melt: the importance of temperature and plagioclase composition, with implications for terrestrial and lunar magmatism. Geochim Cosmochim Acta 206:273–295. https://doi.org/10.1016/j.gca.2017.03.003

Tait SR, Jaupart C (1992) Compositional convection in a reactive crystalline mush and melt differentiation. J Geophys Res 97:6735–6756

Tait SR, Huppert HE, Sparks RSJ (1984) The role of compositional convection in the formation of adcumulate rocks. Lithos 17:139–146

Tsuchiyama A (1985) Dissolution kinetics of plagioclase in the melt of the system diopside-albite-anorthite, and origin of dusty plagioclase in andesites. Contrib Mineral Petrol 89:1–16

Vance JA (1965) Zoning in igneous plagioclase: patchy zoning. J Geol 73(4):636–651. https://doi.org/10.1086/627099

Voigt A, Cassidy M, Castro JM, Pyle DM, Mather TA, Helo C, Abdurrachman M, Kurniawan IA (2022) Experimental investigation of Trachydacite Magma Storage Prior to the 1257 eruption of Mt Samalas. J Petrol 63:1–19. https://doi.org/10.1093/petrology/egac066

Wager LR, Brown GM, Wadsworth WJ (1960) Types of igneous cumulates. J Petrol 1(1):73–85

Waters LE, Lange RA (2015) An updated calibration of the plagioclase-liquid hygrometer-thermometer applicable to basalts through rhyolites. Am Mineral 100:2172–2184

Weber G, Blundy J (2024) A machine learning-based thermobarometer for magmatic liquids. J Petrol 65:egae020. https://doi.org/10.1093/petrology/egae020

Weinstein SA, Yuen DA, Olson PL (1988) Evolution of crystal-settling in magma chamber convection. Earth Planet Sci Lett 87:237–248

Wiebe RA (1973) Relations between coexisting basaltic and granitic magmas in a composite dike. Am J Sci 273:130–151

Wiebe RA (2016) Mafic replenishments into floored silicic magma chambers. Am Mineral 101:297–310. https://doi.org/10.2138/am-2016-5429

Wiebe RA, Snyder D (1993) Slow, dense replenishments of a basic magma chamber: the layered series of the Newark Island layered intrusion, Nain, Labrador. Contrib Mineral Petrol 113:59–72

Winslow H, Ruprecht P, Gonnermann HM, Phelps PR, Munoz-Saez C, Delgado F, Pritchard M, Amigo A (2022) Insights for crystal mush storage utilizing mafic enclaves from the 2011–12 Cordón Caulle eruption. Sci Rep 12:9734. https://doi.org/10.1038/s41598-022-13305-y